Title

Advancing Two-photon Lithography by Integrating Microfluidics and Optical Tweezers

Author

Chizari, Samira

Publication Date

2020

UNIVERSITY OF CALIFORNIA

Los Angeles

Advancing Two-photon Lithography by Integrating Microfluidics and Optical Tweezers

A dissertation submitted in partial satisfaction of the
requirements for the degree Doctor of Philosophy
in Mechanical Engineering

by

Samira Chizari

2020

ABSTRACT OF THE DISSERTATION

Advancing Two-photon Lithography
by Integrating Microfluidics and Optical Tweezers

by

Samira Chizari

Doctor of Philosophy in Mechanical Engineering

University of California, Los Angeles, 2020

Professor Jonathan B. Hopkins, Committee Co-Chair

Professor Yong Chen, Committee Co-Chair

This doctoral work aims to advance two-photon lithography (TPL) using a hybrid approach that integrates TPL with microfluidics (MF) and optical tweezers (OT) to enable unprecedented microstructures. The hybrid additive manufacturing system (i.e., when two or more systems act on the same site simultaneously or sequentially) developed in this work is able to automatically fabricate complex three-dimensional microstructures with multi-material designs and nanoscale resolution. The Ph.D. research communicated in this dissertation focuses on exploiting the full potential of TPL to provide unparalleled microfabrication capabilities by pursuing: (1) Scanning two-photon continuous flow lithography (STP-CFL); TPL is supplemented with microfluidics to allow for high throughput fabrication of 3D arbitrary-shaped microparticles with multi-material designs. (2) Simultaneous printing and deformation of microsystems via TPL and holographic optical tweezers to create microstructures with embedded strain energy. (3) Automated 3D engineered microgranular crystal fabrication, where an advanced hybrid approach is realized by integrating TPL with both MF and OT.

The dissertation of Samira Chizari is approved.

Dino Di Carlo

Xiaochun Li

Jonathan B. Hopkins, Committee Co-Chair

Yong Chen, Committee Co-Chair

University of California, Los Angeles

2020

Dedicated to Maman & Baba.

Table of Contents

List of Figures

Acknowledgments

1.1. **Family**

I would like to express my deepest gratitude to my caring mother, Ashraf, and my loving father, Mohammad. I have no doubt I could not have achieved any of my life accomplishments without your endless love and support. You were there for me every single time I needed you and repeatedly encouraged me to believe in myself and fear nothing! You cried with me out of joy and sadness during all these past years. I cannot thank you enough, no matter how hard I try!

Next, I would like to thank my sister, Sara, for her unconditional love and support. You are a true source of inspiration! I have learned a lot from you and am continuously amazed by your beautiful soul. I am so grateful for your presence in our lives! Also, a big kudos to my brother-in-law, Navid, for being such a patient partner when I talked with Sara for hours!

I also would like to thank my brother, Alireza. Frankly, I would not be writing this thesis to get my Ph.D. from UCLA if it were not for you! I clearly remember the day you took me on a UCLA campus tour with Sean and encouraged me to apply! Since the very first day I entered the USA, you were there for me every time I asked without fail! I am forever thankful for your big heart and kindness.

Finally, I would like to thank my best friend and lovely husband, Amin, who happens to be my lab mate! Amin joon, you are the best partner-in-crime! No matter what crosses my mind, you are down for it! From our unplanned crazy trips to late-night research experiments in the lab, you have always shown up! I cannot imagine myself any happier than I am with you! Me’ si!

P.S. A million thanks to my in-laws: Mahnaz, Parviz, and Matin, for their limitless love and support from thousands of miles away.

1.2. **UCLA**

First and foremost, I want to thank my prudent and kindhearted adviser, Professor Jonathan Hopkins. You always trusted in me and my capabilities and continued to encourage me even when I doubted myself. Thank you so much for being a great listener and a fantastic adviser for me, both professionally and personally.

Next, I would like to thank my dear friend, labmate, and mentor, Luke! I will never forget our fun days in the lab making all sort of wacky stuff, our coffee breaks when we discussed literally everything, our diligent search for free food events, particularly the ones with swags (CS teatime to be specific), our Farsi lessons, and most importantly: “Lucky Luke Learns Farsi” YouTube channel! I appreciate your kind support during all these years, and I believe your friendship is the most precious swag I’ve got in “Elexible” Research Group. Kudos to Cameron for introducing me to you in the first place.

I also would like to express my gratitude to my other fantastic labmates: Michael, Miles, Ryan, Rodolfo, Adam, Frederick, Sydney, James, and Peter. Thanks for all the wonderful memories and your help! Also, I want to thank my collaborators: Dr. Dan Stoecklein, Shreya, and Prof. Di Carlo at UCLA, as well as Dr. Robert Panas, Dr. Andrew Pascall, and Dr. Maxim Shusteff, for their dedication and support.

Last but not least, I acknowledge Prof. Kavehpour for believing in my capabilities and recommending me for UCLA admission, and Prof. Chen for giving me the opportunity to work in his lab the summer before starting my Ph.D.

1.3. **Friends**

First and foremost, I want to thank Abolfazl and Navid, the first and best Persian friends I made in the USA! Our friendship started on the MAE orientation day, strengthened in Prof. Kim’s class, and has carried on since then! Guys, thank you for being there for me during the highest and lowest points of my time at UCLA. I will forever remember the days I ran to your office to tell you the good news and the times I called you when I couldn't handle the bad news alone.

I would like to also thank so many other great friends: my 14+3 & MYZS people, Hamed, Aysan, and Marzieh, for having my back and cheering me on in this journey.

1.4. Funding

National Science Foundation Graduate Research Fellowship generously supported this work (Grant No. DGE-1650604); Without this fellowship, my Ph.D. journey would have become much more challenging; Additionally, my research was supported by UCLA Mechanical and Aerospace Engineering Departmental Fellowship; Airforce Office of Scientific Research (Grant No. FA9550-15-1-0321, FA9550-18-1-0459), and Department of Energy via Presidential Early Career Award for Scientists and Engineers (Grant No. B620630).

1.5. Journals

Chapter 1 contains the background sections of Chizari, S., Udani, S., Farzaneh, A., Stoecklein, D., Di Carlo, D., Hopkins, J.B., "Scanning Two-Photon Continuous Flow Lithography for Fabrication of Multi-functional Microparticles," Optics Express, 28.26 (2020): 40088-40098. SC wrote the manuscript; DD *et al.* revised it.

Chapter 1 contains the background sections of Chizari, S., Shaw, L.A., Hopkins, J.B., 2019, "Simultaneous Printing and Deformation of Microsystems via Two-Photon Lithography and Holographic Optical Tweezers," Materials Horizons, 6(2): pp. 350-355. SC wrote the manuscript; LS and JH revised the manuscript.

Chapter 2 is a version of Chizari, S., Udani, S., Farzaneh, A., Stoecklein, D., Di Carlo, D., Hopkins, J.B., "Scanning Two-Photon Continuous Flow Lithography for Fabrication of Multi-functional Microparticles," Optics Express, Accepted November 2020. SC wrote the manuscript; DD *et al.* revised it.

Chapter 3 is a version of Chizari, S., Shaw, L.A., Hopkins, J.B., 2019, "Simultaneous Printing and Deformation of Microsystems via Two-Photon Lithography and Holographic Optical Tweezers," Materials Horizons, 6(2): pp. 350-355. SC wrote the manuscript; LS and JH revised the manuscript.

Chapter 3 contains some parts on microscale fabrications of the microstructures from:

Song, Y., Panas, R.M., Chizari, S., Shaw, L.A., Mancini, J.A., Hopkins, J.B., Pascall, A.J., 2019, "Additively Manufacturable Micro-Mechanical Logic Gates," Nature Communications, 10: 882. SC wrote the manuscript of sections used.

Shaw, L.A., Chizari, S., Dotson, M.B., Song, Y., Hopkins, J.B., 2018, "Compliant Rolling-contact Architected Materials for Shape Reconfigurability," Nature Communications, 9: 4594. SC wrote the manuscript of sections used.

Chapter 4 is a version of Chizari, S., Lim, M. P., Shaw, L. A., Austin, A. S., Hopkins, J. B., 2020, "Automated Optical-tweezers Assembly of Engineered Microgranular Crystals," Small: p.2000314. SC wrote the manuscript; JH *et al*. revised the manuscript.

Chapter 4 contains the Optical Tweezing section of Behera, D., Chizari, S., Shaw, L.A., Porter, M., Hensleigh, R., Xu, Z., Roy, N.K., Connolly, L.G., Zheng, X., Saha, S.K., Hopkins, J.B., Chen, S-C., Cullinan, M.A., "Current Challenges and Potential Directions Towards Precision Microscale Additive Manufacturing – Part II: Laser-Based Trapping, Curing and Heating Processes," submitted to Precision Engineering, 2020. SC wrote the section used here, LS, MP, and JH edited it. Other co-authors on the paper wrote different parts of the review paper, which are not used in this thesis.

Vita

2010 - 2014	Bachelor of Science in Mechanical Engineering Khajeh Nasir Toosi University of Technology, Tehran, Iran
2015 - 2017	Master of Science in Mechanical Engineering University of California, Los Angeles (UCLA) Mechanical & Aerospace Engineering (MAE) Department, Los Angeles, USA Graduate Fellows, Research and Teaching Assistant
2017 – 2020	Co-founder & Co-president, MAE Graduate Council (MAEGC) at UCLA
2017 – 2020	Co-founder & Social and Outreach Co-chair, Iranian Graduate, and Professional Association (IGPA) at UCLA
2017 - 2020	National Science Foundation Graduate Research Fellowship Program (NSF GRFP) Fellow
Summer 2017	Optomechanical Engineering Intern, NASA Jet Propulsion Laboratory (JPL), Pasadena, USA
2018 – 2019	Social Media Chair, UCLA Engineering Graduate Student Association (EGSA)
Summer 2019	Hardware Engineering Intern, Apple Inc., Sunnyvale, USA
2017 - 2020	Doctor of Philosophy Science in Mechanical Engineering UCLA MAE, Los Angeles, USA Major: Microelectromechanical Systems & Nanotechnology Minor: Design and Manufacturing
2020 – present	MEMS Research & Development Engineer, Microfabrica Inc. Van Nuys, USA

Journal Publications

Chizari, S., Udani, S., Farzaneh, A., Stoecklein, D., Di Carlo, D., Hopkins, J.B. 2020, "Scanning Two-Photon Continuous Flow Lithography for Fabrication of Multi-functional Microparticles," Optics Express, 28.26 (2020): 40088-40098.

Chizari, S., Behera, D, *et al.*, "Current Challenges and Potential Directions Towards Precision Microscale Additive Manufacturing – Part II, III & IV," Precision Engineering (2020).

Chizari, S., *et al.*, "Automated Optical-tweezers Assembly of Engineered Microgranular Crystals," Small (2020): 2000314.

Chizari, S., *et al.*, "Simultaneous Printing and Deformation of Microsystems via Two-Photon Lithography and Holographic Optical Tweezers," Materials Horizons 6(2) (2019): 350-355.

Song, Y., Panas, R.M., **Chizari, S.**, *et al.*, "Additively Manufacturable Micro-Mechanical Logic Gates," Nature communications 10.1 (2019): 1-6.

Shaw, L.A., **Chizari, S.**, *et al.*, "Compliant Rolling-contact Architected Materials for Shape Reconfigurability," Nature communications 9.1 (2018): 1-12.

Shaw, L.A., **Chizari, S.**, Hopkins, J.B., 2018, "Improving the Throughput of Automated Holographic Optical Tweezers," Applied Optics 57(22): pp. 6396-6402.

Shaw, L.A., **Chizari, S.**, *et al.*, "Scanning Two-photon Continuous Flow Lithography for Synthesis of High-resolution 3D Microparticles," Optics Express, 26(10) (2018): 13543-13548.

Shaw, L.A., **Chizari, S.**, *et al.*, J.B., "Holographic Optical Assembly and Photopolymerized Joining of Planar Microspheres," Optics Letters 41(15) (2016): 3571-3574.

Chapter 1. Introduction

1. Motivation

Two-photon lithography (TPL) is a non-linear photopolymerization process [1] (Figure 1.1) that has found widespread application in additive manufacturing of complex, true three-dimensional microarchitectures (Figure 1.2) owing to its high resolution and adaptability to different materials such as polymers [2], metals [3], and ceramics [4]. This doctoral research aims to provide unprecedented 3D microfabrication capabilities that facilitate the manufacturing of the next generations of microsystems and metamaterials by overcoming certain limitations of TPL, including 1) single material printing at a time and low throughput, 2) inability to in situ actuation and concurrent deformation of printed structures, 3) inability to assemble and join microsystems.

Addressing these issues augments TPL microfabrication capabilities and significantly expands its application areas. TPL, in its current state, is a powerful technique for fabricating complex 3D microstructures with nanoscale resolution for high precision applications, such as photonic crystals,

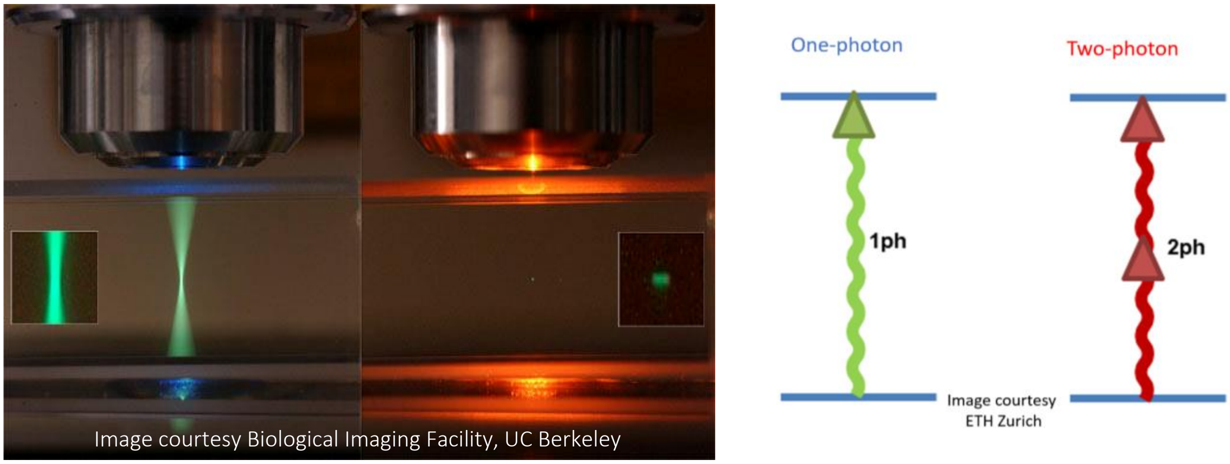

Figure 1.1 One-photon vs. two-photon absorption.

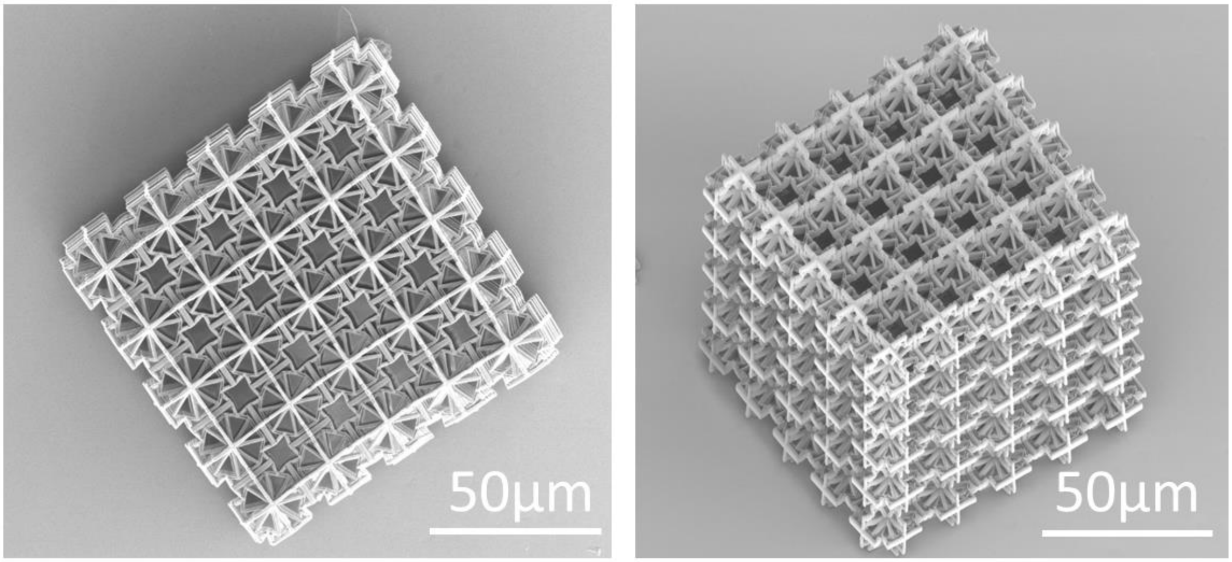

Figure 1.2 5x5x5 lattice of negative Poisson’s coefficient metamaterial fabricated by the custom TPL system developed in this Ph.D. work

cell culture structures, and architected metamaterials. Nevertheless, many other applications can benefit from the unique capabilities of TPL. Still, they either cannot be achieved without the contribution of complementary methods or can dramatically improve in terms of resolution and throughput if a hybrid approach is utilized. Therefore, this work aims to advance two-photon lithography via integration with microfluidics and optical tweezers to enable unprecedented microstructures (Figure 1.3).

2. Background

2.1. Flow lithography using microfluidics

Extensive applications of custom microparticles have fueled the research and technology development of approaches required to fabricate them. One promising technique for fabricating such particles is microfluidic lithography that uses liquid prepolymer resin, which flows in a microchannel in conjunction with a light source to induce photopolymerization of the

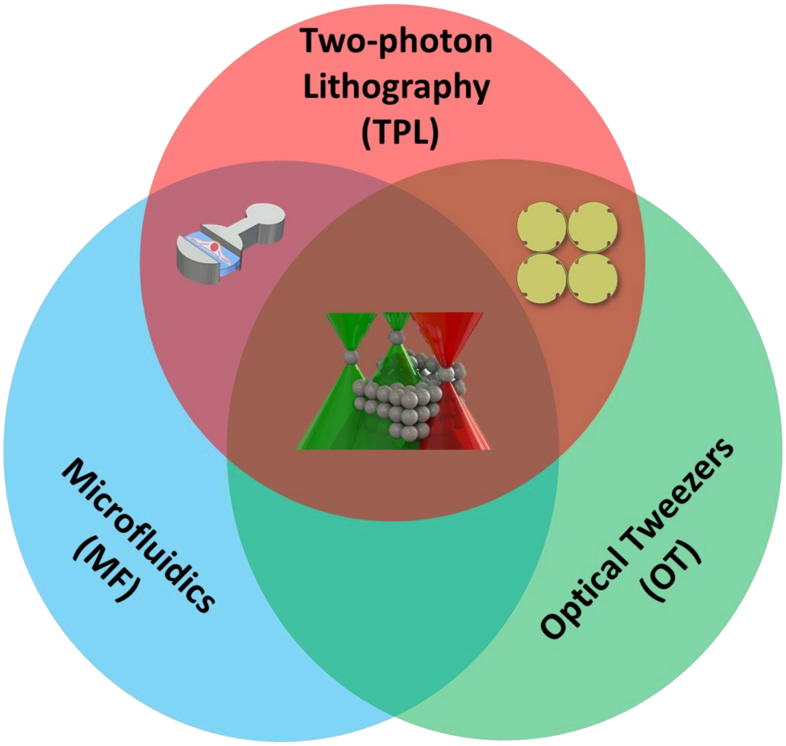

Figure 1.3 Technologies used in the hybrid microfabrication approach of this work.

microparticles. Spherical [5] or slightly deformed spherical (i.e., disk or rod) [6]microparticles were the most common geometries that could be achieved in early forms of this technique because they could be fabricated using droplet microfluidics. In this method, droplets of photosensitive materials are generated by suspension in an immiscible fluid in a microchannel. These droplets are then exposed to light with a wavelength that initiates the photopolymerization process required to solidify them [7]. Using the same approach, slightly deformed spherical microparticles could also be achieved by varying the design of the microchannels. For example, disc-shaped microparticles have been achieved by flattening the droplets in wide and short channels before curing them [6].

To further diversify the shapes of microparticles, conventional lithography techniques were coupled with microfluidics-based fabrication, and continuous flow lithography (CFL) was introduced [8]. This method used a microfluidic channel with a steady flow of photocurable resin and an ultraviolet (UV) source that is exposed to certain regions of the microchannel through an optical mask, which produces solid microparticles that are extrusions of the mask patterns. However, the printing resolution of this technique was low, especially at the edges of microparticles, as the flow caused smearing. This smearing occurred because the duration of polymerization was accompanied by significant motion of the prepolymer solution. To overcome this issue, low flow rates were inevitably used, which sacrificed system throughput. To achieve better shape accuracy and higher throughput, a follow-up method called stop-flow lithography (SFL) was introduced [9] with the same procedure, except that the flow was stopped during the exposure step. After polymerization, the flow resumed to wash the microparticles and flow in fresh resin to the fabrication site. This technique also yields extruded versions of 2D patterns on the mask but has a higher resolution and throughput, which depends on the size of the particle and the channel. A variation of SFL uses opaque magnetic microparticles in the resin to induce a gradient in the UV light at the exposed areas, thus enabling nonlinear curing along the axial direction [10]. Building off of CFL and SFL, lock-release lithography [11] was introduced in which positive features on the microchannel were used as molds to add constraints to the geometry of the particles made by projection lithography. Particles were subsequently released by pressure-induced channel deformation. This method allows for multiple medium exchanges or multi-material patterning of the particles as they can be fixed in place during the process.

Despite the high throughput of these systems, each has limitations in terms of geometry and shape of the particles that can be fabricated. In addition, the height of the microparticle depends on the channel geometry as the polymerization process is not localized axially, which causes the light to cure the whole column of exposed photopolymer. The improved vertical resolution was achieved by implementing optofluidic maskless lithography that uses a digital micro-mirror device (DMD) to project patterns on a membrane-mounted channel, with the channel height being controlled by applying pressure on the membrane [12]. This method can be used in a layer-by-layer fashion to achieve 3D microparticles. By changing the medium between steps, multi-material particles are also made possible. One disadvantage of this approach, however, is that it requires complex microfluidics. A similar layer by layer approach, called vertical flow lithography [13], uses a microfluidic device with four symmetric horizontal inlets and one vertical outlet, allowing for more fabrication flexibility in terms of material distribution within each layer. Thus, tapered shapes can be achieved within layers using this approach. This technique has a throughput of 4 particles per minute, which is low compared to previously discussed state-of-the-art SFL. Recently, the same approach was used to fabricate micro-tubes [14] in vertical channels using two-photon lithography, which dramatically enhanced the resolution.

Another technique that deviates from layer-by-layer fabrication but still uses projection lithography is called optical transient liquid molding [15], in which photopolymer resin streams are shaped by software-aided inertial flow engineering [16] to fabricate microparticles with concurrent UV exposure through a mask. In this technique, a fully-3D microparticle shape is formed by the union of two extruded 2D shapes: one shape from the optical mask and the other from the sculpted flow. However, this method is limited in terms of particle size (⩾ 100 µm) and complexity, as one of the extruded 2D shapes is restricted to what is possible through inertial flow sculpting [16].

All of the approaches discussed above are based on projection lithography and one-photon polymerization, which cannot achieve submicron resolution. Two-photon polymerization can address this issue in that it localizes the polymerization to small portions of the laser’s focal point that are above the threshold for nonlinear two-photon absorption, resulting in printing resolution of less than 100 nm. Usage of two-photon polymerization in microfluidic lithography was first demonstrated by Lasa *et al.* [17]. This group fabricated bi-material micro springs in a stream of two co-flowing photopolymers by moving a piezoelectric stage in a circular motion as the polymers flowed past a fixed laser spot. Despite the high resolution of the microparticles created by this method and its ability to create multi-material particles, the method is limited in terms of i) throughput, which is estimated to be 0.2 particles per minute and is governed primarily by the speed of the piezoelectric stage [13], ii) particle size, which is governed by the speed of the mechanical laser shutter, and iii) particle geometry complexity, which is governed by the ability to compensate for the flow velocity. However, these issues were addressed in chapter 2 of this Ph.D. dissertation, where scanning two-photon continuous flow lithography (STP-CFL) technique is presented.

2.2. **Optical Tweezing in TPL-based microfabrication**

Optical Tweezing (OT) (also called trapping) [18] is a powerful technique that has been widely used by biologists to manipulate nano- and micro-sized objects [19]. This technique has also found applications in microfabrication due to its high precision in positioning microparticles [20,21]. By incorporating a diffractive optical element called a spatial light modulator (SLM), holographic optical tweezing (HOT) becomes possible. The HOT approach uses a single laser source to generate multiple optical traps that can be independently and simultaneously reconfigured [22]. In this work, a new system is introduced that integrates both the TPL and HOT approaches to allow microelements to be simultaneously printed and deformed to fabricate new polymer microsystems that could not be made using any other approach.

Existing works have utilized TPL-based fabrication and HOT-based manipulation as serial processes in separate systems, such as in the micro-snap-fit mechanism [23] and the micro-screw-wrench[24] by Köhler *et al.*, micro-assembly of non-spherical particles by Ksouri *et al.*[25], and the optical waveguides by Palima *et al.* [26]. Separate TPL and HOT systems are difficult to use because they require challenging post-processing steps to develop the printed objects without washing them away (e.g., complex cage structures are often printed in addition to the intended objects to contain them [24,27]). Furthermore, such systems require the cumbersome task of locating the printed micro-objects under the HOT system after development to then manipulate them. In addition to being difficult to operate, separate TPL and HOT systems are inherently not capable of printing embedded strain energy within structures. The reason is that such systems cannot print new features onto existing objects while they are being deformed by optical tweezers to passively hold the objects in their deformed state and thereby trap the optically induced strain energy within their geometry.

Although others have developed TPL systems integrated with optical-tweezing capabilities (e.g., the system that fabricated the microscale tetherball pole by Dawood *et al.* [28] or the system that enabled the delivery and encapsulation of microspheres in polymer by Askari [29]), no one has combined TPL with HOT. The published integrated systems are only capable of generating a single optical trap to deform printed structures—not multiple independently controlled traps, which HOT systems are capable of generating. As a result, such systems are limited by how they can deform the objects they print. Such objects must be fixed to substrates in order to deform their geometry because a single optical trap produces only a single force, which would displace a free-floating object—not deform it. Additionally, the current integrated systems have not demonstrated the ability to print embedded strain energy within fabricated objects in part because this capability requires sophisticated simulation and automation algorithms to synchronize the TPL and optical tweezing capabilities. The current systems have also only demonstrated the handling of spherical objects. Spherical objects possess the easiest geometry to manipulate using optical tweezers because a sphere requires only one trap to handle and the optimal location to place that trap is commonly known to be at the spheres' centre. Handling other arbitrarily shaped objects in a controlled way often requires multiple optical traps placed at nonintuitive optimal locations to produce the forces and moments required for moving and deforming the object to the desired location and orientation. It is important that these locations and orientations are precise since they must correspond with the location and orientation of new features that must subsequently be printed in conjunction with the previously printed and deformed objects to passively hold them in place and thereby store embedded strain energy. The system introduced in chapter 3 combines TPL and HOT for the first time in a single integrated system to address the aforementioned shortcomings, thus enable the fabrication of microsystems with embedded strain energy.

3. Dissertation Overview

Chapter 2 articulates the high-throughput fabrication of 3D microparticles using a scanning two-photon continuous flow lithography (STP-CFL) technique in which microparticles are shaped by scanning the laser beam at the interface of laminar co-flows. The results demonstrate the ability of STP-CFL to manufacture high-resolution complex geometries of cell carriers that possess distinct regions with different functionalities. A new approach is presented for printing out-of-plane features on the microparticles. The approach eliminates the use of axial scanning stages, which are not favorable since they induce fluctuations in the flowing polymer media, and their scanning speed is slower than the speed of galvanometer mirror scanners.

Chapter 3 demonstrates simultaneous printing and deformation of polymer microsystems using an integrated TPL and HOT approach. This approach is the first of its kind to enable the fabrication of advanced metamaterials, micromechanisms, soft microrobots, and sensors that require embedded strain energy in their constituent compliant elements to achieve their intended behaviors. We introduce a custom-developed photopolymer chemistry suitable for near-infrared TPL fabrication but remains unreactive in the visible-light regime for HOT-based handling. We facilitated the optimal HOT-based actuation of TPL-fabricated microsystems by advancing a ray-optics-based optical-force simulation tool to work with microbodies of any arbitrary shape. We demonstrate this integrated system's utility via fabrication of three unique case studies, which could not be achieved using any alternative technologies.

Chapter 4 presents a scalable, automated approach for fabricating three-dimensional (3D) microgranular crystals consisting of desired arrangements of microspheres using holographic optical tweezers and two-photon polymerization. The ability to position microspheres as desired within lattices of any configuration allows designers to engineer the behavior of new metamaterials that enable advanced applications (e.g., armor that mitigates or redirects shock waves, acoustic lenses for underwater imaging, damage detection, and non-invasive surgery, acoustic cloaking, and photonic crystals). Currently, no self-assembly or automated approaches exist with the flexibility necessary to place specific microspheres at specific locations within a crystal. Moreover, most pick-and-place approaches require the manual assembly of spheres one by one and thus do not achieve the speed and precision required to repeatably fabricate practical volumes of engineered crystals. In this paper, the rapid assembly of 4.86 μm-diameter silica spheres within differently packed 3D crystal-lattice examples of unprecedented size using fully automated optical tweezers is demonstrated. The optical tweezers independently and simultaneously assemble batches of spheres that are dispensed to the build site via an automated syringe pump where the spheres are then joined together within previously unattainable patterns by curing regions of photocurable prepolymer between each sphere using two-photon polymerization.

Chapter 5 concludes this Ph.D. dissertation with a brief summary and an overview of the hybrid TPL-based technology created in this work.

Chapter 2. Scanning two-photon continuous flow lithography for fabrication of multi-functional microparticles

1. Custom Microparticles

Micro- and nanoparticles are recognized as versatile research tools in the fields of cell studies [30,31], drug delivery [32–34], self-assembly [35,36], barcoding [37], encoding [38,39], and anti-counterfeiting [40]. Particle-based cell culture and manipulation platforms are particularly promising as they could enable breakthrough applications in single-cell analysis and selection. For example, self-steering microparticles can act as carriers for cells [30] in continuous flow cytometers or imaging flow cytometers, improving the ability to analyze morphological features in a potential cell or microtissue/organoid-based therapies in a high-throughput manner. Such microparticle carriers containing cells of interest can be recovered following rapid analysis and machine intelligence directed sorting [41], obviating current challenges in selecting cells from surfaces in standard microscopy systems. To develop cell carriers to be effective in cell culture and high-throughput sorting, it is essential to be able to control the size and shape of the microparticles, as well as their chemical composition, to improve cell adherence to specific regions of interest on each microcarrier. The size of a microcarrier and the nature of its cell-adherent surface dictates whether the carrier will be useful in single-cell studies. Prior work in creating microcarriers for high-throughput cell analysis used microcarriers many times larger than the target cells (~400 µm compared to ~10 µm cell size) [30], which would be limited to multi-cell aggregates or cell cluster studies. In addition, the geometry of cell carriers can be utilized to protect adhered cells while tuning the carrier's hydrodynamic behavior. Microcarriers that passively self-align in the flow could eliminate the need for active measures (e.g., magnetic fields) or complex fluidic components (multiple confining 3D co-flows) to orient the carrier, which helps ensure

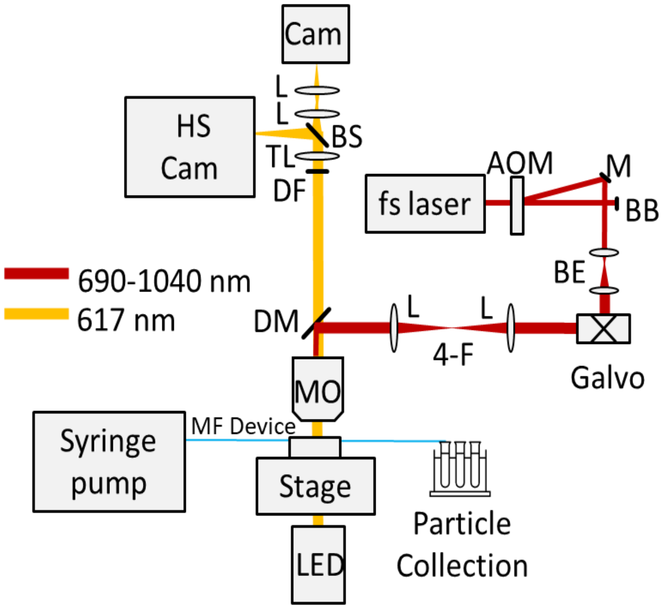

Figure 2.1 STP-CFL system schematic. The system uses a high-speed camera (HS Cam), lenses (L), a beam splitter (BS), a tube lens (TL), a dichroic filter (DF), a dichroic mirror (DM), a 4-F telescope (4-F), galvanometer mirrors (Galvo), a beam expander (BE), a beam block (BB), an acousto-optic modulator (AOM), a femtosecond pulsed laser (fs), a mirror (M), a microscope objective (MO), a microfluidic device (MF), and a light emitting diode (LED).

uniform cell velocities for consistent imaging [30]. Reducing the need for outside mechanisms of control can lead to increased throughput, as analysis and sorting channels can be more easily parallelized, ultimately enabling the biomanufacturing of cells and microtissues at scales relevant for therapeutic applications. Finally, precise control over chemically functionalized regions of the microcarrier can be used to design the location to which cells adhere. This multi-material fabrication ability allows for patterning adherent cell shelters within the features of the printed particles to protect adhered cells from the environment or fluid shear stress as well as enable drugs to be delivered to targeted cells [42,43].

The goal of this work is to push the limits of flow lithography techniques to meet the aforementioned manufacturing needs of emerging cell-based microcarrier technologies.

2. Scanning two-photon continuous flow lithography

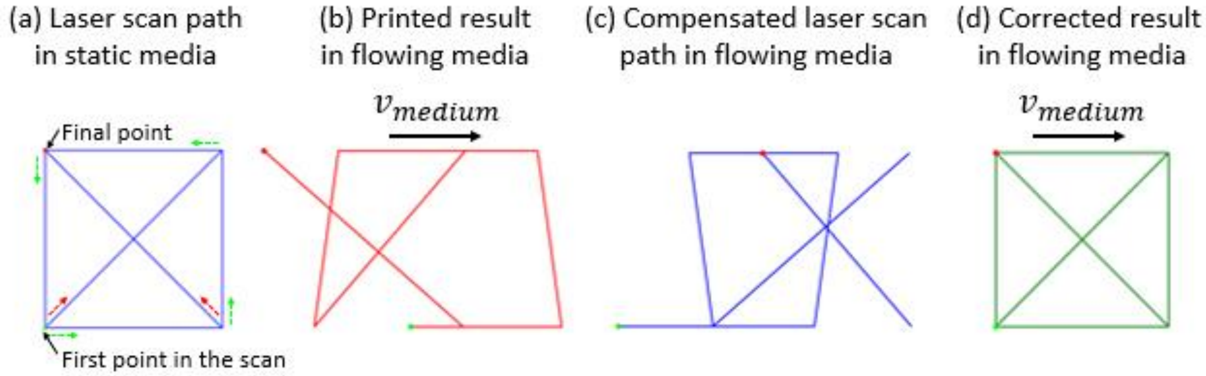
(a) Laser scan path in static media
(b) Printed result in flowing media
(c) Compensated laser scan path in flowing media
(d) Corrected result in flowing media

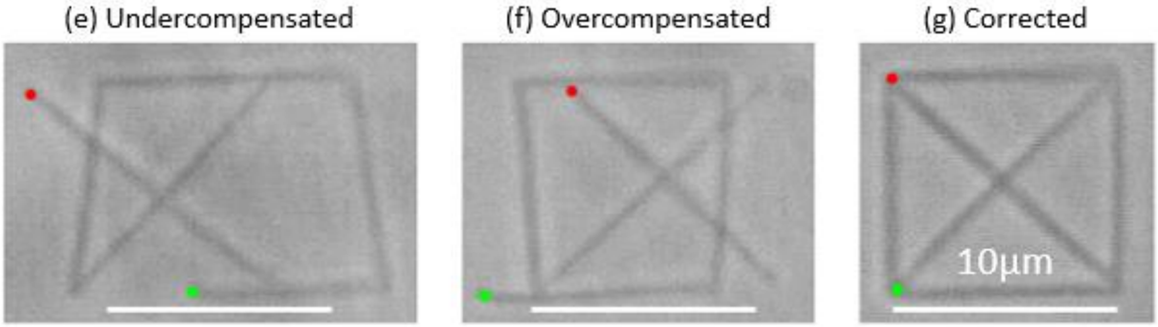
(e) Undercompensated
(f) Overcompensated
(g) Corrected

Figure 2.2. Laser scan path correction for STP-CFL [44]

In STP-CFL (enabled by the system shown in Figure 2.1) [44], galvanometer mirrors are used to rapidly scan a femtosecond pulsed laser beam in a continuous flow of resin such that the laser follows the microparticle and compensates for its continual movement while it is being printed (Figure 2.2). To perform this flow compensation, first, the flow velocity is determined by taking successive images of a flowing microparticle at a known time difference. It is worth noting that

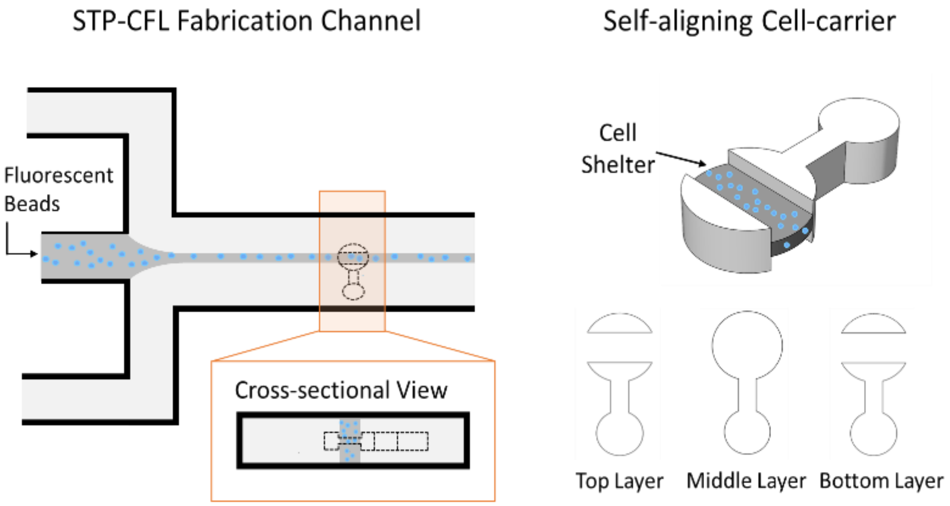

Figure 2.3 Schematic of microfluidic channel used for bi-functional STP-CFL (left) and design of cell carrier with distinct shelter area (right). Lengths are not to scale.

due to the small size of fabricated microparticles, a uniform velocity profile was assumed across each microparticle. Next, the laser scan path is updated by shifting each scan point downstream, considering its position in the path, the scan rate, and the flow velocity. This technique also allows for the layer-by-layer fabrication of arbitrary 3D shaped microparticles by synchronized movement of the galvanometers for XY plane scanning and piezoelectric stage for Z-axis scanning of the laser focal point. We utilized an acousto-optic modulator to rapidly attenuate or turn off the laser beam entirely. We demonstrated the fabrication of single material particles of approximately 10 µm in size, at the rate of 31 two-dimensional particles per second. This throughput is comparable to the rates reported for projection lithography techniques such as SFL; however, STP-CFL results in an order of magnitude higher resolution. The 3D particles were fabricated at the rate of 15 microparticles per second, which is currently unrivaled by other two-photon lithography-based techniques.

In this work, we advance the capabilities of the STP-CFL technique to realize multi-functional microparticles by printing at the interface of two or more co-flowing streams of prepolymer resins that contain different components. Furthermore, we introduce a new printing approach to achieve out-of-plane features of these microparticles without axial scanning of the laser spot. We demonstrate this technique by fabricating bi-functional microparticles with the geometry of self-aligning single-cell carriers. The asymmetric dumbbell shape of this design (Figure 2.3) allows for their self-alignment in Stokes flows [45,46]. Moreover, the 3D architecture these microparticles encompass is designed to have a sheltered area to protect cells from the shear stress experienced in downstream analysis workflows, such as microfluidic-based flow cytometry platforms. To ensure the cells only adhere to the shelter area, a bi-functional structure is needed in which cell-adhesive material is exclusively used in the shelter region. STP-CFL is well-suited to fabricate such cell carriers due to its ability to fabricate custom 3D microparticles at the scale of a single cell. In addition, by including co-flows of different polymer precursors in the fabrication channel, multi-functional microparticles are made possible.

3. Materials

The liquid prepolymer solution consists of 99% w/w poly (ethylene glycol) diacrylate (PEGDA Mn~575; Sigma-Aldrich) as the monomer, and 1% w/w Irgacure 369 (BASF) as the photoinitiator. To provide a proper visual demonstration of the bi-functional microparticle fabrication capability of STP-CFL, blue fluorescent microspheres of size 0.5 µm (Fluoro-Max, ThermoFisher) were included in the precursor solution of the middle flow to produce the shelter region.

3.1. **Fabrication**

To create the three co-flows required for STP-CFL of the cell carrier microparticles (Figure 2.3), three-inlet microchannels (width=1200 µm, depth=130 µm) were created using soft lithography methods. SU-8 2100 negative photoresist was used to fabricate the master mold for the microchannels on silicon wafers (UniversityWafer, Inc.), using a standard photolithography process. Polydimethylsiloxane (PDMS) elastomer and the curing agent (Sylgard 184, Dow Corning) were mixed at a 10:1 ratio by weight, poured onto the mold, degassed, and then cured at 65°C overnight. After cutting and peeling the device, 1.5 mm holes were punched at the inlets and outlet. The PDMS and No. 1 thickness cover glass (Electron Microscopy Sciences) were air plasma treated (Plasma Cleaner, Harrick Plasma) and bonded to create an enclosed microchannel. Tygon tubing (OD = 0.06”) was used to connect the microchannel inlets to 1 mL plastic syringes (BD) that were controlled using a syringe pump (Chemyx Fusion 100) to stabilize the location and width of the co-flows, a Y-connector (IDEX Health and Science) was used to split a single flow from the syringe pump driven at 7 µL/min to shape the two outer flows, and the middle flow was driven at 0.05 µL/min to shape a narrow stream of approximately 10 µm wide (Figure 2.4).

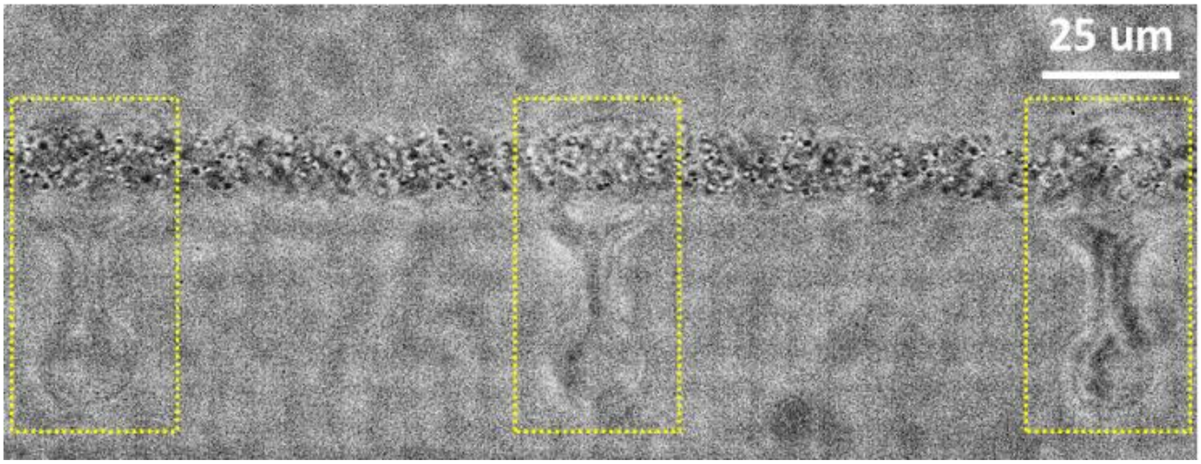

Figure 2.4 Optical image of the high-speed camera depicting STP-CFL of cell carrier microparticles in three laminar co-flows (see Video 1).

To precisely monitor the fabrication process at high flow rates in the channel, the primary STP-CFL system [44] was upgraded with a Phantom VEO-440 highspeed camera to produce the work of this paper. We also updated the flow velocity measurement method that runs before each round of microparticle printing: the prepolymer medium is exposed to the static laser spot for 50ms, which results in a solidified line of photopolymer in the channel (Figure 2.5). By measuring the length of this line, the flow velocity is determined (ranging between 500-1300 µm/s based on the flow rate), and the code automatically updates the scanning data to compensate for the movement of microparticles in the channel while they are being printed.

Since the desired cell carriers are about five times larger than the microparticles in our original STP-CFL work, each particle's scan data contains considerably more scanning points. As a result, each particle travels a longer distance during polymerization, and at the same time, may be exposed to larger velocity gradients in the channel due to the presence of Poiseuille flow conditions. It was observed that the velocity gradient could exert moments on the microparticles in a way that the layers would misalign during the fabrication (Figure 2.6). To resolve this issue, we utilized wider (1200 µm versus 200 µm) and deeper (130 µm versus 50 µm) channels and printed at the middle planes of each dimension to achieve a minimal velocity gradient across the particle.

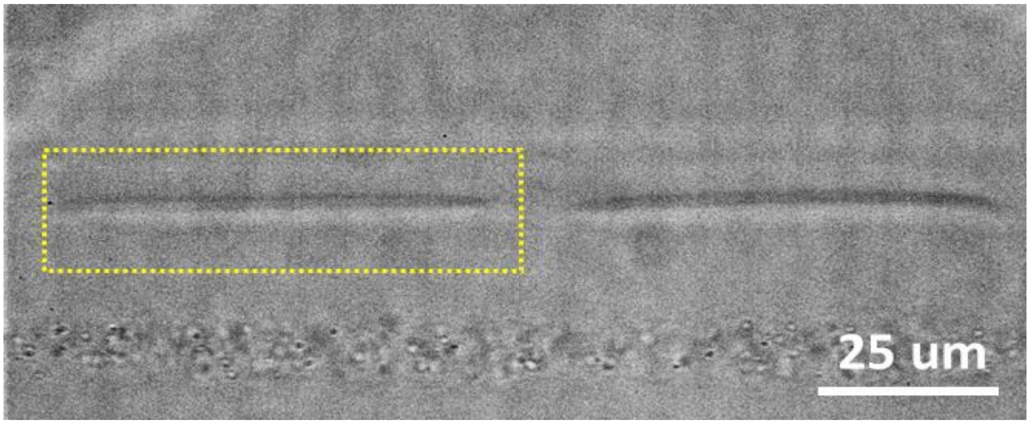

Figure 2.5 Line printed by exposing the flowing medium to a static laser beam to measure flow velocity.

To print the out-of-plane features of the shelter region with high resolution, we present an alternative approach to the axial scanning of the stage. This new method relies on the fact that the out-of-plane thickness of a printed voxel in two-photon polymerization is correlated with the exposure time of the laser beam at any given location [47]. Therefore, in the absence of a z-scanning stage, out-of-plane features can be created by tuning the exposure time (i.e., point density) in different regions. To utilize this method, we first slice the cell carrier geometry into three layers stacked in the z-direction (Figure 2.3). Then we use STP-CFL to scan the points in each layer without moving the laser spot out of the plane. Consequently, the thickness of different regions grows in proportion to the laser exposure time at each point. Eliminating the Z-stage scanning is beneficial as it could introduce flow perturbations and limits overall throughput due to the lower scan rate of piezoelectric stages when compared to scanning mirror galvanometers. This new technique also allows for continuous variation of thickness in applications where rough surfaces created by stage stepping are not favorable [47]. It is worth noting that microparticles that can be

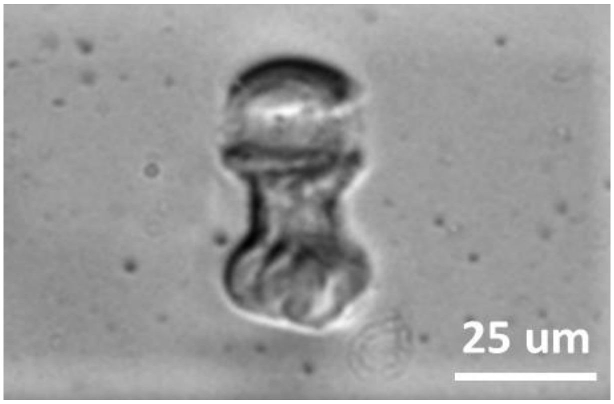

Figure 2.6 Brightfield image of a poorly fabricated microparticle resulting from the velocity gradient induced movement of the microparticle in the channel during fabrication.

fabricated with the presented approach are axially symmetric and cannot be hollow. Particles deviating from these rules can be fabricated with our original STP-CFL approach published in [44].

3.2. **Microparticle Recovery**

Immediately after microparticle fabrication, the contents of the collection tube (microparticles along with precursor solution) were passed through a 10 μm cell strainer (CellTrics), followed by a 0.1% (w/v) Pluronic F-127 in phosphate-buffered saline solution (PBSP) in order to remove excess microspheres for imaging purposes. Next, the cell strainer was flipped, and microparticles were recovered by flushing with more PBSP. PBSP was also used to pre-coat all tubes, pipette tips, and the strainer to reduce microparticle loss through adsorption to the plastic surfaces.

3.3. **Confocal and Fluorescence Microscopy**

Unreacted acrylate groups of cell carrier microparticles were modified with biotin groups after fabrication by reacting microparticles in PBSP with 0.44-0.55 mg/ml of Acrylate-PEG-Biotin

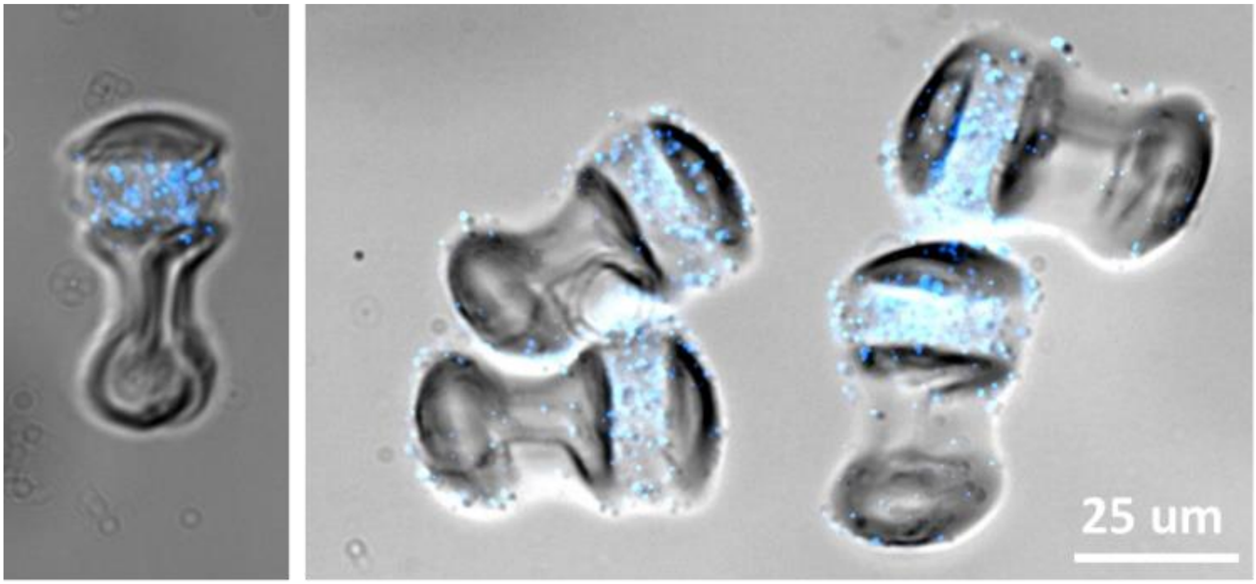

Figure 2.7 Fluorescent microscopy of cell carriers after post-processing. Images indicate the fluorescent bead pattern is aligned with the cell-shelter region. Measurements indicate ~10% of increase in dimensions due to swelling of the hydrogel microparticles.

(MW = 5000, Nanocs) with a final concentration of 0.072-0.091% lithium phenyl-2,4,6-trimethylbenzoylphosphinate (LAP) photoinitiator. The Acrylate-PEG-Biotin reaction vial was exposed to UV light (15.5 mW/cm2, Omnicure S2000) for one minute while being stirred. Microparticles were then washed three times, incubated with Streptavidin conjugated with Alexa Fluor 568 (Invitrogen) for 15 minutes to allow the orthogonal binding of biotin to Alexa Fluor 568 Streptavidin, and then washed again. This post-fabrication modification allows the entire microparticle, in addition to the blue microsphere embedded shelter region, to be imaged using confocal microscopy.

Confocal images of cell carrier microparticles in coverglass wells were taken on a Leica SP8 confocal microscope using a 40x oil immersion objective. The 405 nm laser was used to image the blue fluorescent microbeads embedded in the shelter region of microparticles. The 552 nm laser was used to image the entire Alexa Fluor 568 Streptavidin-coated microparticle body. Z stacks with a step size of 0.34 or 0.5 µm were taken, and the 3D reconstruction of each microparticle was clipped along the major axis to reveal the cross-section. Heights of the shelter region and adjacent region were extracted manually on ImageJ.

Microparticles were also imaged using fluorescence microscopy (Figure 2.7) to allow for higher throughput image acquisition for basic features such as microparticle length (Figure 2.8) and bead localization. Free microparticles were imaged in PBSP on cover glass using an inverted microscope (Nikon, Eclipse Ti - S fluorescence microscope) with a 40x objective lens in brightfield and DAPI channel (Figure 2.7). Alexa Fluor 568 Streptavidin modified microparticles were also imaged in the TRITC channel, and the binary signal from this channel was used to measure microparticle major axis length using a custom MATLAB code.

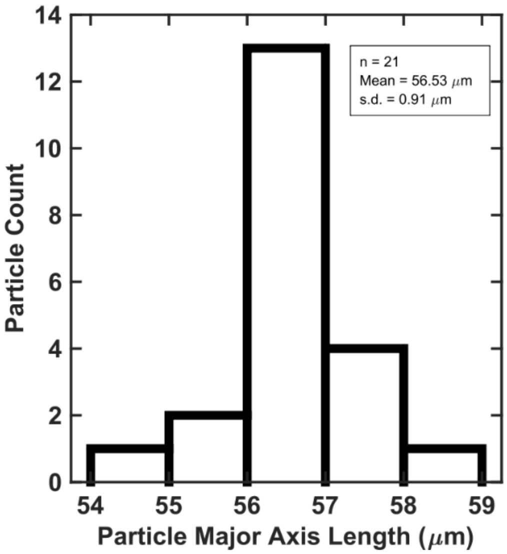

Figure 2.8 Cell carrier microparticle length distribution based on fluorescence microscopy images.

4. Results and Discussion

A 10x slowed down movie of the fabrication process is provided in Video 1, where cell carrier microparticles of size 50 µm (measured using optical microscopy) are printed with a throughput

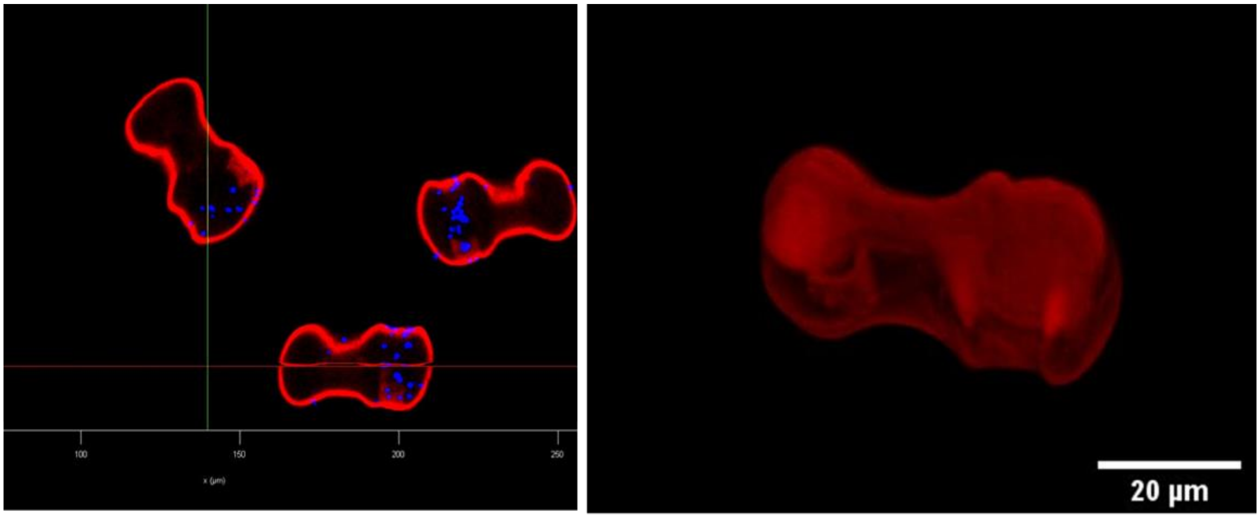

Figure 2.9 Confocal microscopy of cell carriers. Cross-section view of the cell carriers (left) and the 3D render of the microparticle (right).

of 10 microparticles per second using a femtosecond pulsed laser with 20 mW of power at 690 nm. The beam is scanning the points of the scan path at 15 kHz using the galvanometer mirror system. We have demonstrated the maximum throughput of the system by printing the cell carrier microparticles in flows with velocities as high as 1300 μm/s, but we note that the maximum flow rate and throughput of the STP-CFL technique are now limited by the scan rate of the galvanometer mirrors. Consequently, the maximum rate of microparticle fabrication is directly proportional to the size and number of points in the scan path of each microparticle. By utilizing faster galvanometer mirrors, it would be possible to increase fabrication throughput for a given microparticle geometry. In addition, the characteristic microparticle dimension can conceivably be as large as the field of view, which is currently 200 μm by 180 μm in our system. However, the goal of this work was to perform multi-material particle fabrication at a length-scale similar in size to adherent cells, which we successfully achieved.

By exploiting the exposure time at different regions of the cell carrier microparticles during fabrication, we were able to produce microparticles with height variation along with a custom 2D outline, opening the possibility of rapid manufacturing of complex 3D shaped microparticles. In this case, we were able to create a cell shelter region with a length-scale matching many adherent cell types (~10-15 um), with a sheltered depth of ~1.5 µm based on cross-sectional data obtained via confocal microscopy (Figure 2.9). Compared to the height of the region adjacent to the cell shelter, the shelter region was measured to be 18-24% shorter depending on the power density used by the laser during fabrication. This height difference can be further tuned by changing the point density in the sliced 3D microparticle geometry at each region based on the desired design. This kind of height tunability is a powerful and unique feature of the new STP-CFL approach presented in this work, significantly improving the fidelity in replicating subtle microparticle geometries. We envision that this could be utilized for designing modular microcarrier "parts" that protect different cell types and morphologies or even purposely expose the cells to as-designed fluid shear stress.

In addition to more complex geometry at sub-100 µm length-scales, we demonstrate the ability to create multi-functional microparticles through the introduction of precursor coflows using multiple inlets that lead to a single straight fabrication channel. We illustrated this using fluorescent microbeads in the middle stream to define the shelter region (see Figure 2.3, Figure 2.4, and Figure 2.7). Small molecules can also be added in the future to allow for a cell-adhesive composition that is contained within the shelter region, provided that (i) mass diffusion of the added molecules does not significantly alter the designed distribution before the particles have polymerized, and (ii) the cross-linked matrix of the hydrogel particle effectively retains the dopant (e.g., through steric interaction, covalent bonds, or other means). We note that the flowing streams should have similar material properties (i.e., density and viscosity) to achieve reliable steady-state behavior both in flow and after the particles are fabricated, minimizing the effects of fluid-fluid and fluid-structure interaction on the two-photon polymerization. Current multi-material formulations for bio-compatible microcarriers predominantly use similar PEG-based hydrogels, so we do not anticipate this being an issue for our intended application. However, the range of usable material differences (e.g., two immiscible polymers) should be explored in future work.

Funding

Air Force Office of Scientific Research (FA9550-18-1-0459); Presidential Early Career Award for Scientists and Engineers (N00014-16-1-2997, B620630); National Science Foundation (DGE-1650604).

Acknowledgment

We acknowledge the use of the Integrated Systems Nanofabrication Cleanroom at the California NanoSystems Institute (CNSI) at UCLA. Confocal laser scanning microscopy was performed at the CNSI Advanced Light Microscopy/Spectroscopy Shared Resource Facility at UCLA.

Chapter 3. Simultaneous Printing and Deformation of Microsystems via Two-photon Lithography and Holographic Optical Tweezers

New technologies have been evolving rapidly to enable the fabrication of microsystems currently not feasible to make using conventional methods. Of particular interest are microsystems that require the storage of strain energy in their compliant constituent elements to facilitate new kinds of metamaterials, micro-mechanisms, soft micro-robots, and other compliant microarchitectures. General systems that possess embedded strain energy often exhibit unique non-linear characteristics such as negative and/or tunable stiffness [48] and show behaviors such as buckling, snapping, and wrinkling. Although such behaviors have typically been avoided when designing traditional systems due to their nonlinear complexities, these behaviors have more recently been exploited for enabling more advanced applications [49]. Sensor, actuator, and switch applications have, for instance, been achieved by leveraging the configuration changes that dramatically occur when some multi-stable strain-energy-storing systems are subjected to small perturbations [50]. Much research has been conducted toward enabling such embedded-strain-energy applications on the macroscale; however, limitations in fabrication technologies have prevented the realization of such systems on the microscale. In this work, we present a new technology that combines two-photon lithography (TPL) with holographic optical tweezers (HOT) to enable the fabrication of micro-sized systems with embedded strain energy.

The presented TPL/HOT system can simultaneously print multiple microelements of any shape (either free-floating or fixed to a substrate), reorient and hold them in place in a suspension of photopolymer resin, and deform them in a coordinated effort using multiple forces and moments imposed on the elements by groups of automated optical traps. Our approach requires no intermediate chemical development procedure between the TPL and HOT steps, allowing the print-and-deform process to be synchronized and automated. Thus, subsequent features can be printed on top of previously printed features to passively store strain energy in their geometry as optical tweezers are simultaneously holding them in precisely deformed configurations.

To facilitate and optimize the handling, deformation, and actuation of the polymer structures printed by our system, custom-developed photopolymer chemistry is introduced in this paper. The photopolymer chemistry is notable for its two-photon absorption in the near-infrared (NIR) range, transparency to 532 nm visible light, and readily available chemical components, which enable printing and deformation of the polymer microsystems fabricated.

We also present an advanced geometric optics tool that generates optical force and torque profiles on micro-bodies of any shape. Simulating such loads has been an area of interest since the discovery of optical tweezers. These simulations are categorized according to the wavelength of the laser beam (λ) and the diameter (D) of the particle being trapped. If a particle is more than an order of magnitude smaller than the wavelength of the laser beam (D<<λ, Rayleigh regime), Lorentz force expressions on point dipoles can be used to calculate the induced optical forces [51]. For particles comparable in size to the wavelength of the laser beam (D∼λ, Mie regime), more rigorous methods are required to simulate the induced optical forces. One popular method is the *T-matrix* formulation [52] developed by Nieminen *et al.* [53]. Another method, which uses optical force density principles to achieve the same objective, was recently introduced by Phillips *et al.* [54] to provide a more straightforward alternative. Although these and other methods are capable of simulating optical forces imposed on particles of any shape, they are limited to Mie-regime scenarios. For scenarios of interest to the contributions of this paper in which the printed body is much larger than the wavelength of the trapping laser by at least an order of magnitude (D>>λ, geometric optics regime), ray tracing techniques can be employed to simulate optical forces imposed [55]. Although these techniques have primarily been used to simulate the forces imposed on spherical bodies, others have successfully used ray tracing techniques to simulate the forces imposed on semi-spherical objects such as ellipsoids [55], semi-cylindrical rods[56], and Janus spheres [57]. Ray tracing techniques have been used to simulate the optical forces imposed on bodies of arbitrary shapes [58–60], but defining the geometry of such shapes is typically cumbersome and limited to shapes that can be analytically defined manually. Often times, those shapes are approximated for the sake of simplicity, and thus the accuracy of the results is compromised. We extend the ray-tracing toolbox provided by Jones *et al.* [60] to simulate the accurate optical forces imposed on bodies of any shape that pertain to the geometric-optics regime and are defined using standard computer-aided design (CAD) software, which can be uploaded to the tool as standard stereolithography (*.stl)* files. This tool enables our integrated TPL/HOT approach to rapidly identify the optimal trap locations on printed bodies of arbitrary shapes to deform them in an automated way for embedding strain energy within microsystems, which were not previously possible to fabricate.

1.1. **Materials**

We present a new photopolymer resin that is cured by two-photon absorption using NIR (760 nm) femtosecond pulses but is unreactive to visible continuous-wave (CW; 532nm) light used for optical trapping. The resin consists of 1.1%wt. TPO-Li (Colorado Photopolymer Solutions), 38.4%wt. ethoxylated (15) trimethylolpropane triacrylate (Sartomer SR9035), and 60.5%wt. deionized (DI) water. The refractive index of the liquid polymer was measured to be 1.3918, and the refractive index of the solid polymer was measured to be 1.4912, a difference significant enough to produce the optical refraction and momentum transfer needed to support optical trapping as shown in the Simulation section. The resin chemistry was initially inspired by Dawood *et al.*, who used synthesized MBS as the photoinitiator [28]. However, we present a resin with a commercially available photoinitiator, TPO-Li as a substitute to MBS, which renders the hybrid TPL/HOT process more widely accessible.

1.2. **Microfabrication**

The microsystems are fabricated in a sample chamber consisting of a microscope slide and a coverslip separated by two pieces of tape of approximately 50 μm thickness each. The microscope slides were functionalized with acrylate for better adhesion of the polymer bodies printed [28]. The hybrid microfabrication process includes printing with TPL and manipulation using HOT, and if required, one or both of these processes are repeated to complete the fabrication process.

The hybrid microfabrication process can be run fully automated. The MATLAB software developed for the control of the TPL/HOT system correlates multiple inputs, including *(1)* the lithography file (in .*stl* format) representing the structure to be printed, *(2)* the desired locations of the optical traps on the printed bodies, *(3)* printing parameters (e.g., scan rate and laser power), and finally *(4)* calibration values that relate the position and scaling of the scanning mirrors' area, projected hologram's area, and recorded images. This information is loaded into a MATLAB graphical user interface (GUI) using a .*mat* file, and the system handles subsequent fabrication steps automatically.

1.3. **Simulation**

In this section, a ray-optics-based simulation capable of calculating optical forces and moments on microsystems with any arbitrary shape is developed and presented here. This tool (available to download at "https://www.flexible.seas.ucla.edu/software") is an extension of the open-source and validated Optical Tweezers Software (OTS) published by Jones, Maragò, and Volpe [60], but has been advanced here to accept general .*stl* files, to define the geometry of general shapes. The presented MATLAB code facilitates the modeling of complex microstructures without the need to manually define different surfaces and their coordinates, which can be a very time-consuming and challenging task for surfaces that are not basic geometric shapes. The improved tool is important because it allows for *a priori* knowledge of where to optimally place optical traps to manipulate and strain TPL-printed parts of arbitrary shape.

In order to demonstrate the capabilities of the simulation tool, optical forces on the irregularly shaped body shown in Figure 3.1a-b are studied. The body simulated in the figure is fabricated as an embedded-strain-energy lattice case study and is discussed later in the Fabrication section. Simulation results show that in-plane optical trapping forces are maximized at the edges of the printed micro-bodies due to refraction at those edges (Figure 3.1a-b). This refraction and resulting momentum transfer produce a stable potential well that attracts the body to the focal spot of the laser. Furthermore, the simulation tool reveals that, for planar TPL-fabricated microsystems, there is an optimal trapping plane located within the bounds of the microsystem in which axial forces are zero and stable (i.e., 375 nm above the mid-plane of the free-floating body as shown in Figure 3.1c), and therefore, optical traps can effectively move the body in-plane without rotating it out of plane. This principle is leveraged in the operation of the TPL/HOT system in that the optical traps are focused slightly above the TPL writing laser's focal spot. Thus, traps are automatically created at the zero-axial-force mid-plane of the printed micro-bodies immediately after they are printed. Furthermore, simulation data shows that the strongest optical trapping occurs at locations where physical edges are located in close proximity. Since physical edge features result in extremum in the force profile, close placement of opposite edge features creates a sign change and steep slope that results in strong and stable trapping (Figure 3.1c). However, while optical traps placed on thin features generally support strong optical trapping, it also creates a narrow optical force profile that is not stable over a large range. We favored 3µm-wide features as they were observed to balance optical trap strength with stability.

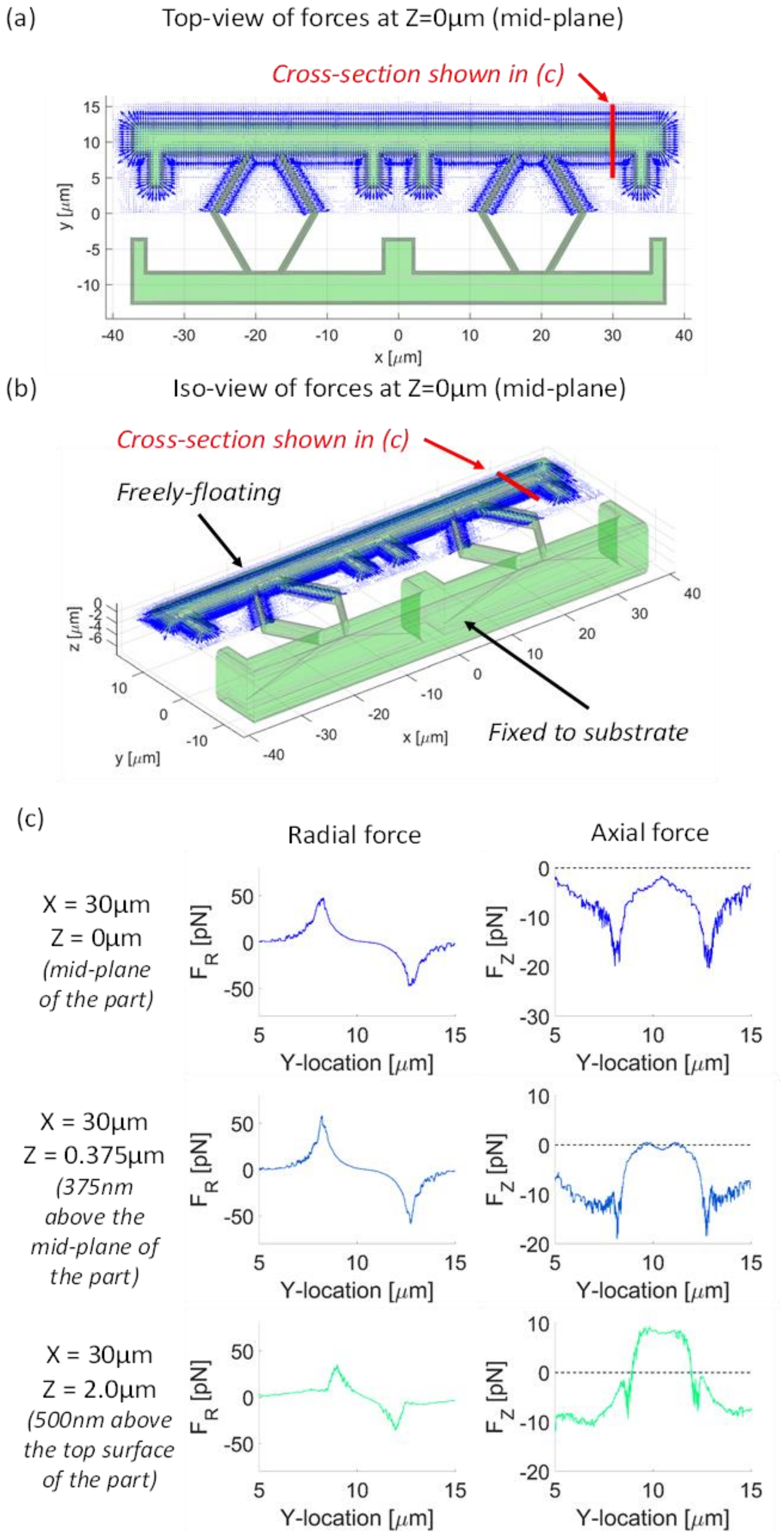

Figure 3.1 Ray-optics-based force simulations on an irregularly shaped body using a 50mW, 532 nm optical trap. The effective numerical aperture of the optical trap is 1.3, the refractive index of the medium is 1.3918, and the index of the micro-body is 1.4912. (a) The top view of the force vector field located at the mid-plane of the free-floating half of the body shows forces are maximized at edges. (b) The isometric view demonstrates the tool's ability to calculate out-of-plane forces and moments, which are minimized when the trapping beam is focused close to the mid-plane of the free-floating body. (c) Cross-sectional subplots show radial and axial forces at various Z-heights across the red line shown in (a) and (b).

1.4. **Fabrication**

Our fabrication system consists of three subsystems: the TPL system, the HOT system, and the imaging system (Figure 3.2). The TPL, HOT, and imaging subsystems use a 100x oil-immersion microscope objective (MO, Olympus Plan Apo Lambda, NA=1.45) and a three-axis micro-positioning stage (Thorlabs MAX341 and BSC203). The imaging system consists of two cameras (Basler ace acA1300-75gm) at 40x, and 100x magnification, doublet lenses (L), beamsplitters (BS1, 50:50 R:T; BS2, 90:10 R:T), tube lens (TL, Thorlabs ITL200), dichroic filters (DF, ND6.0 at 532 nm and 690-1040nm), and two collimated 617 nm LED illumination sources in both reflection and transmission configurations.

The TPL system includes a femtosecond laser (fs laser, Spectra-Physics MaiTai eHP DS), acousto-optic modulator (AOM, IntraAction ATM-802DA2 and ME-820-6), two low-dispersion mirrors (M), beam block (BB), beam expander system (BE, f=50 and 200 mm lenses), 2D scanning mirror galvanometer (galvo, Thorlabs GVS012), 4-F telescope relay (two f=60 mm lenses), power sensor (Thorlabs S142C and PM100USB), and longpass dichroic mirror (DM2, λ_c=650nm). The AOM and two-axis scanning mirror galvanometer are driven by an analog output module (National Instruments NI-9263). In-plane scanning is performed by the two-axis scanning mirror galvanometer, and the sample is translated layer-by-layer using the micropositioning stage.

The HOT system includes a 532 nm continuous wave (CW) laser (Laser Quantum Opus 3W), liquid crystal polarization rotator (LCPR, Meadowlark Optics LPR-100-0532), beam block (BB), polarizing beamsplitter (PBS), beam expander (BE1, f=-50 and 200 mm lenses), mirror (M), 1920-by-1152 pixel phase-only spatial light modulator (SLM, Meadowlark Optics P1920-0532), 4-F telescope relay (f=200 and 250 mm lenses), and shortpass dichroic mirror (DM1, λ_c=567nm). The custom Fresnel beam block the focal plane of the 4-F telescope relay consists of a 200-µm-diameter gold film deposited on a glass coverslip.

To generate the scan path for the TPL laser’s writing spot, a standard computer-aided design (CAD) file is sliced into layers with user-defined thickness, and a G-code scan path is generated for each layer using Slic3r (available at http://slic3r.org/). The G-code commands are then transformed into uniformly-spaced points using a MATLAB script and converted to voltage values for the analog output module that drives the scanning galvanometers.

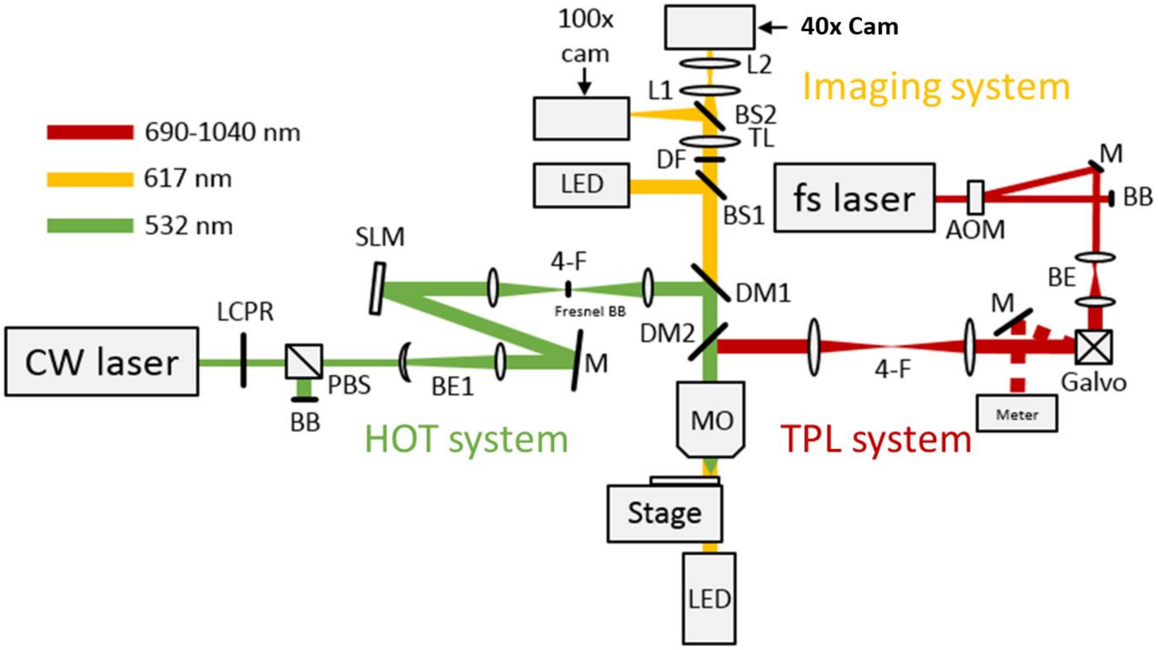

Figure 3.2 Integrated TPL/HOT system schematic.

Four case studies that demonstrate the capabilities of the presented hybrid TPL/HOT system are discussed in what follows.

2. Case studies

2.1. Microscale jack-in-the-box

The *jack-in-the-box* depicted in Figure 3.3a-e and in Video 2 is a proof-of-concept microsystem capable of storing and releasing strain energy. The fabrication process begins with printing five 3μm-thick support layers using TPL (Figure 3.3a) to create a U-shaped box fixed to a substrate. The final layer printed consists of the same U-shaped box but with a vertically oriented lid attached to the box by a compliant hinge as well as a suspended free-floating spring connected to a free-floating disk shaped like a smiley face. The face is then pushed into the box by two optical traps generated by the HOT approach placed on the inner edges of its disk (close to the eyes shown in Figure 3.3b). The box lid is then closed with a single optical trap (Figure 3.3c). The stored energy in the compressed spring and lid hinge is then released by removing the optical traps holding the system in its deformed configuration. The face hits the lid and pushes it open as the strain energy is converted into kinetic energy (Figure 3.3d). Lastly, the lid is brought back to its initial location using a single optical trap, and the structure returns to its initial configuration (Figure 3.3e).

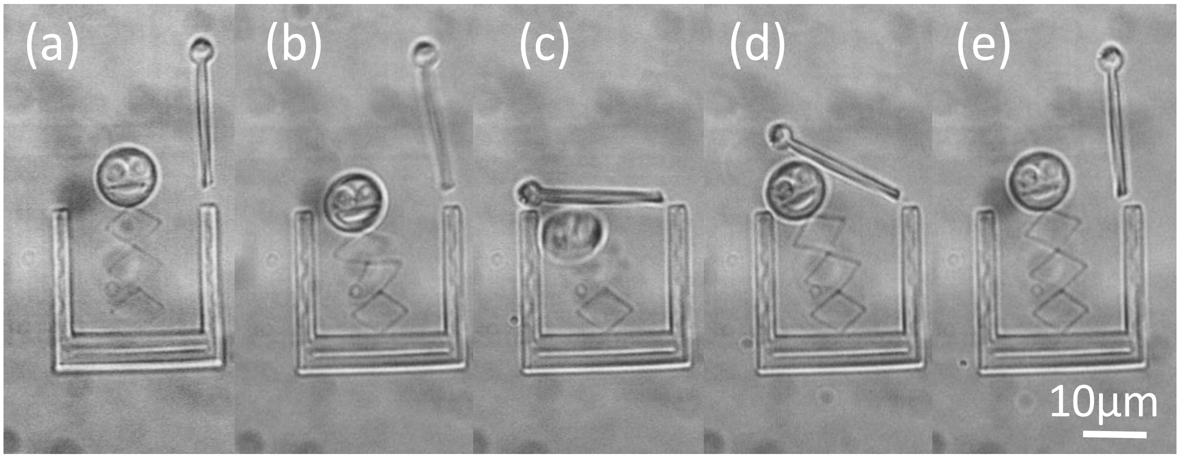

Figure 3.3 Simultaneous printing and deforming of a microscale jack-in-the-box.

2.2. **Embedded-strain-energy lattice**

We now demonstrate the TPL/HOT system's ability to fabricate new metamaterial lattices with embedded strain energy. Such metamaterials could significantly enhance shape-morphing [61], energy absorbing, and deployable [49] applications.

A planar embedded-strain-energy lattice design consisting of 2x2 unit cells was fabricated (Video 3) using our hybrid microfabrication technique in seven steps. First, an undeformed portion of the lattice (i.e., a single pair of unit cells) was fabricated using TPL with one side fixed to the substrate (Figure 3.4a). Second, four optical traps were used to deform the narrow V-shaped flexure elements by actuating the free-floating side of the pair of cells at predefined locations based on *a priori* simulation results (Figure 3.1). Third, the TPL system selectively polymerized the resin at four points at the contact interfaces of the two sides of the cell pair, thus fusing them together (Figure 3.4b). Fourth, the second pair of unit cells was fabricated next to the existing pair using TPL again. The printing location of the second pair of cells was calculated via an image processing routine that uses background subtraction and edge detection in order to find the top of the existing structure. Fifth, the HOT approach was used to bring the second pair of unit cells in contact with the first pair so that the TPL approach can fuse them together (Figure 3.4c). Sixth, four optical traps were again used to deform the V-shaped flexure elements of the second pair of printed cells by actuating their top side at predefined locations, also based on *a priori* simulation results.

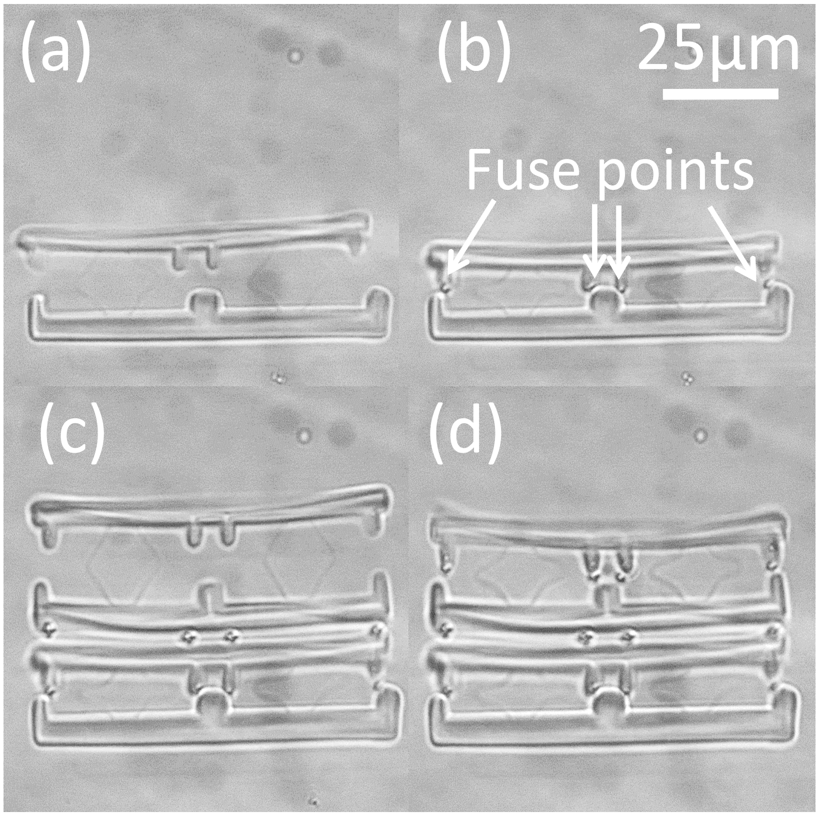

Figure 3.4 Hybrid microfabrication of an embedded-strain-energy lattice consisting of 2x2 cells. Thin, V-shaped flexure elements, which are difficult to see in the figure, join the sides of each cell as shown in Figure 1a-b.

Seventh, the TPL system polymerized resin at four points at the contact interfaces of the two sides of the second pair of cells, thus fusing them together as well (Figure 3.4d).

The result is a fabricated lattice with strain energy stored in deformed portions of its architecture in a stable equilibrium state. Although experimental data [62–64] has shown that, even on the microscale, some of the energy stored in the lattice will likely diminish gradually as the polymer constituent elements undergo stress relaxation, much of the energy is likely to remain stored for practical long-term use. This energy could be suddenly released if the lattice is impacted in such a way that the fuse points (Figure 3.4b) that join the opposing sides of the cells together are cleaved via shearing. Thus, the lattice could cause a projectile that impacts its top surface with sufficient kinetic energy to rebound with even greater kinetic energy after impact. A much larger version of the lattice that consists of many more cells could be used as a shape-morphing or deployable metamaterial that swells in regions that have been fractured. It could also be used as a sensor to detect if and where the impact has occurred. Finally, note that although the lattice of Figure 3.4d is 2D, the hybrid approach introduced here is not limited to the fabrication of planar 2D structures only. 3D versions of the lattice could be designed and fabricated for practical applications.

2.3. **Negative Poisson’s ratio metamaterial**

In our final case study, we apply our new approach to print and actuate a free-floating auxetic (i.e., negative Poisson’s ratio [65]) metamaterial to conduct *in situ* measurements of its Poisson’s ratio. Auxetic metamaterials are important not only because of their unique deformation behavior [66] but also because of other augmented mechanical properties (e.g., resistance to indentation [66] and enhanced energy absorption [67] for use in impact protection devices [68]). In this work, we fabricated a free-floating auxetic lattice via TPL (Figure 3.5a). Six 4μm-diameter disk-shaped features were added to the ends of the lattice to act as handling locations for the HOT approach. The initial and final locations of the six optical traps used to actuate the lattice were predefined, and their displacement was automated so that the Poisson's ratio of the lattice could be measured via image processing (Figure 3.5). The lattice returned to its initial position after removal of the optical traps over numerous cycles due to the strain energy stored in its architecture (Video 4). The boundaries of the lattice were detected using captured images, and the average Poisson's ratio calculated over three cycles, actuated within 30% strain, was found to be -0.54.

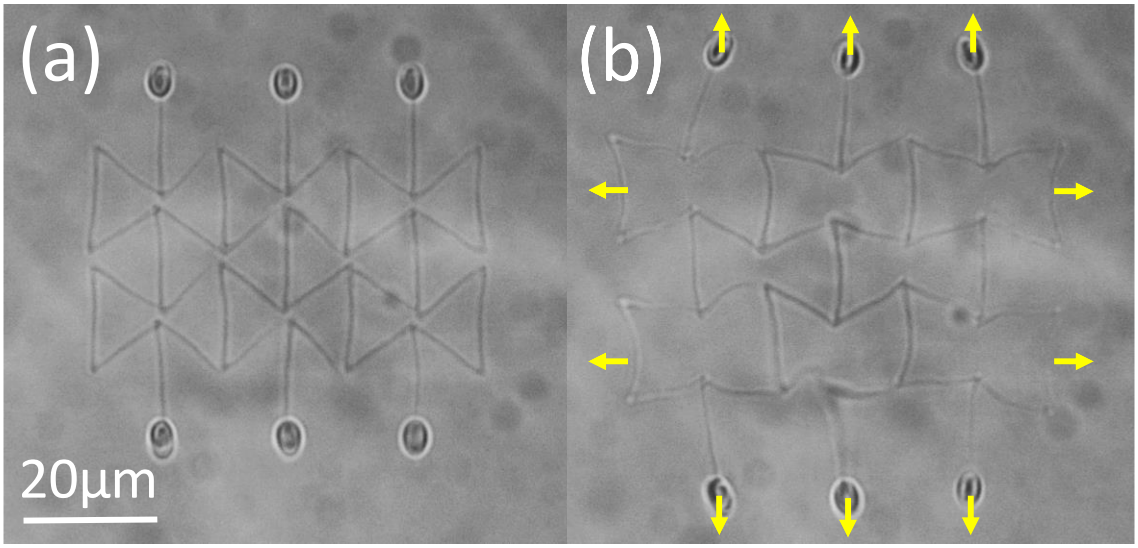

Figure 3.5 (a) A free-floating auxetic lattice printed using TPL; (b) the lattice is actuated using HOT.

2.4. **Microscale Mechanical Logic gate**

Early examples of computers were almost exclusively based on mechanical devices. Although electronic computers became dominant in the past 60 years, recent advancements in 3D micro-additive manufacturing technology provide new fabrication techniques for complex microstructures, which have rekindled research interest in mechanical computations [69,70].

In this section, we introduce the hybrid manufacturing of micro-mechanical logic gates. The proposed mechanical logic gates utilize multi-stable micro-flexures that buckle to perform digital computations based purely on mechanical forces and displacements with no electronic components. A key benefit of the proposed approach is that such systems can be additively fabricated as embedded parts of microarchitectured metamaterials [71] that are capable of interacting mechanically with their surrounding environment while processing and storing digital data internally without requiring electric power.

In order to fabricate the proposed mechanical logic gates at micro-scale, a new approach is proposed that combines the utility of TPL [72] with HOT [73]. In the fabrication process, the TPL approach is used to print polymer structures with submicron resolution, and the HOT approach is used to exert optical forces on the structure to introduce stored strain energy into the flexures. The complete fabrication process was demonstrated for a bi-stable buckling flexure mechanism (Figure 3.6a). First, the CAD model of the bi-stable mechanism was converted into a point cloud, which generated the scan path of a femtosecond pulsed laser in the liquid resin chamber. The undeformed microstructure was then fabricated by the laser at a resolution greater than 600nm. The rigid bodies S and G2 were free to move while the rigid body G1 was fixed to the substrate. Next, two optical traps were created at the ends of the rigid body G2, which pulled G2 into contact with G1. This movement caused the flexures to buckle and deform into one of the stable positions. With the two ends of the rigid bars in contact, they were fused together at the interfaces by locally curing the photopolymer via the TPL approach. To imitate a digital logic signal, the center bar was driven by an optical trap, which switched the bi-stable mechanism between the up position and the down position (Figure 3.6b, Video 5).

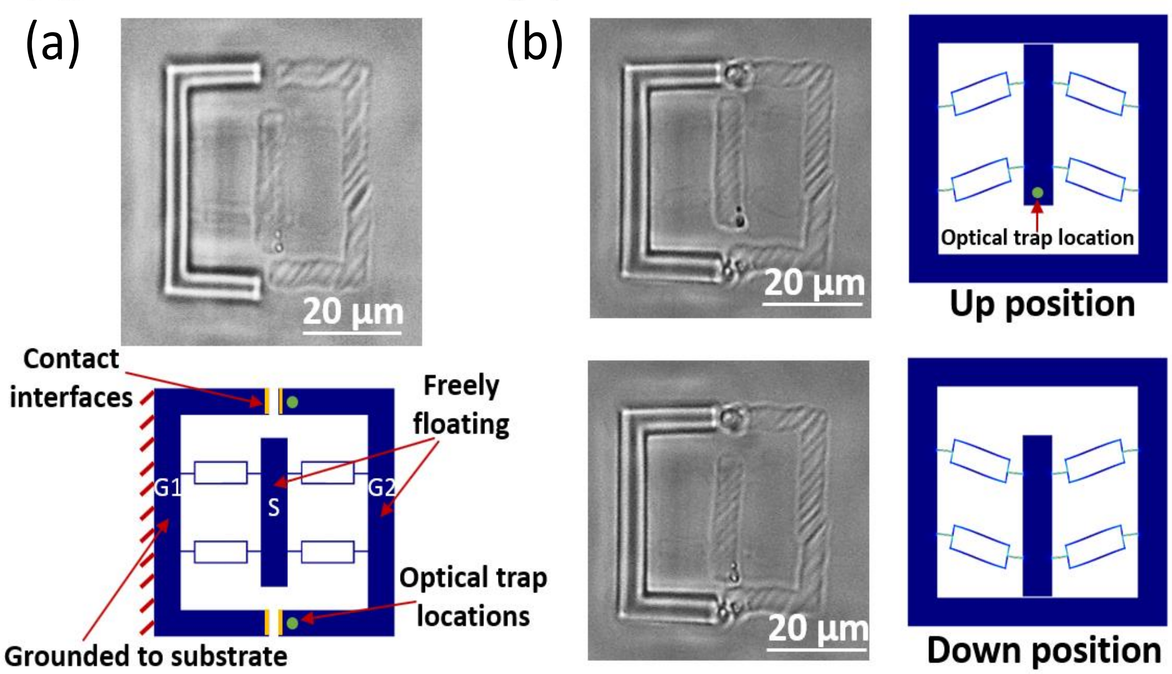

Figure 3.6 Fabrication and experimental testing of the mechanical logic gates. a) Fabrication process of a bi-stable flexure mechanism that combines TPL with HOT. b) A bi-stable flexure mechanism fabricated at microscale that can be driven between two stable positions.

The system shown in Figure 3.1 is used to fabricate the proposed logic gate. The rigid bodies S and G2 were free to move while the rigid body G1 was fixed to the substrate by printing it using TPL on top of five layers of the base structure (Figure 3.6a and Figure 3.7). Then, two optical traps were created at the ends of G2 and pulled G2 into contact with G2. This movement caused the flexures to buckle and deform into their first stable position. With the two ends of the rigid bars in contact, they were fused together by locally curing the photopolymer at the two interfaces via the TPL approach. The final fabricated bi-stable element has an overall size of 38x38x3um and flexure thicknesses of 800nm. An optical trap was used to actuate the center bar, which resulted in the switching of the gate from the "up" position to the "down" position (Figure 3.6).

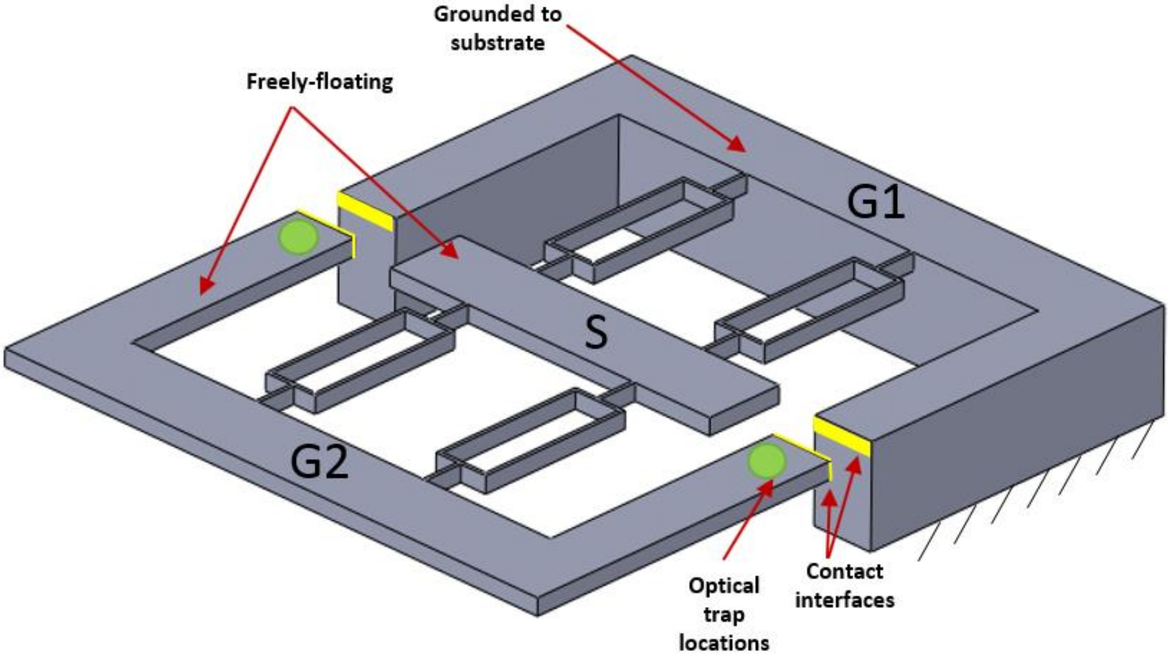

Figure 3.7 CAD model of the bi-stable buckling flexure element printed via TPL.

2.5. **Shape Morphing Compliant Rolling-contact Metamaterials**

Current shape-morphing metamaterials achieve their shape changes by localizing stress concentrations at compliant joints (Figure 3.8a). As the joints are deformed, they increase in strain energy and thus resist the deformation with increasing forces. Furthermore, the areas of high stress tend to break. If compliant rolling-contact joints (CRJ) were used instead, these problems could be avoided. Such joints consist of four identical layers arranged like this (Figure 3.8b). Once assembled, if their initially straight straps are deformed in place, the joint can achieve almost 360 degrees of rotation without ever increasing in stress. If appropriately fabricated, the strain energy remains largely constant no matter how much the joint is rotated and produces near zero stiffness. Thus by using this joint within a lattice, a new metamaterial is created that can deform extreme amounts with low actuation energy. These lattices can be made by assembling multiple identical and monolithic layers (point). They can be made to achieve a single degree of freedom (point), or they can be made to achieve multiple degrees of freedom so that they can take on many different shapes (Figure 3.8c-d).

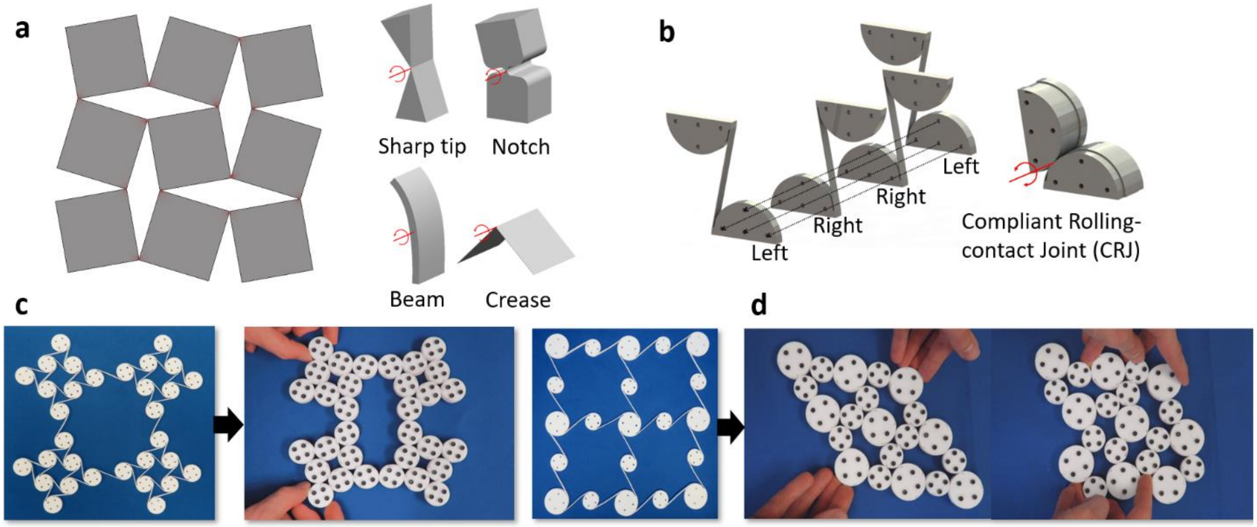

Figure 3.8 (a) Traditonal compliant structures (b) compliant rolling-contact joint (CRJ) is the inspiration for CRAMs. (c,d) Example CRAM structures are shown with circular cams rolled together and can morph to assume many shapes.

One approach (Figure 9-8a) for fabricating CRAMs at the microscale is to make them with flexure straps that are already curled around their cams in an initial strain-free state using TPL only. Such CRAMs would need to be designed with gaps between their straps and cams as well as spacers between their layers (Figure 3.9b) to prevent the resulting lattices from binding due to straps that are fused to their cams. Even if such designs could be perfectly fabricated, however, these gaps would produce slop between the cams, which would drastically lower the resulting CRAM’s compressive and tensile Young’s moduli. Moreover, an unwanted actuation stiffness would exist, which would grow as the cams rotate because their straps would be fabricated with a curved contour in a strain-free state. It is also difficult to fabricate such CRAMs since they either end up with straps that fuse to their cams due to slight over-exposure from the femtosecond laser (Figure 3.9c) or the straps tend to unwrap when they are underexposed (Figure 3.9d). Thus, to fabricate CRAMs at the microscale to achieve their intended behavior, the hybrid TPL/HOT approach is used. The system first leverages its TPL capabilities to print layers of cams connected by initially straight flexure straps. The system then uses its HOT capabilities to generate multiple optical traps that simultaneously impart the necessary loads at different locations on each cam to strategically deform their straps as they float in the original polymer suspension medium. This process is shown for the layers of a CRJ (Figure 3.9e) and a square-tessellated CRAM (Figure 3.9f). Our system has also demonstrated the ability to hold one deformed layer of cams together as another subsequent layer is printed and deformed above or next to it. The system has also shown promise for assembling and fusing such deformed layers using the system’s femtosecond laser to cure the liquid polymer between them. Video 6 is real-time visualizations of the fabrication process.

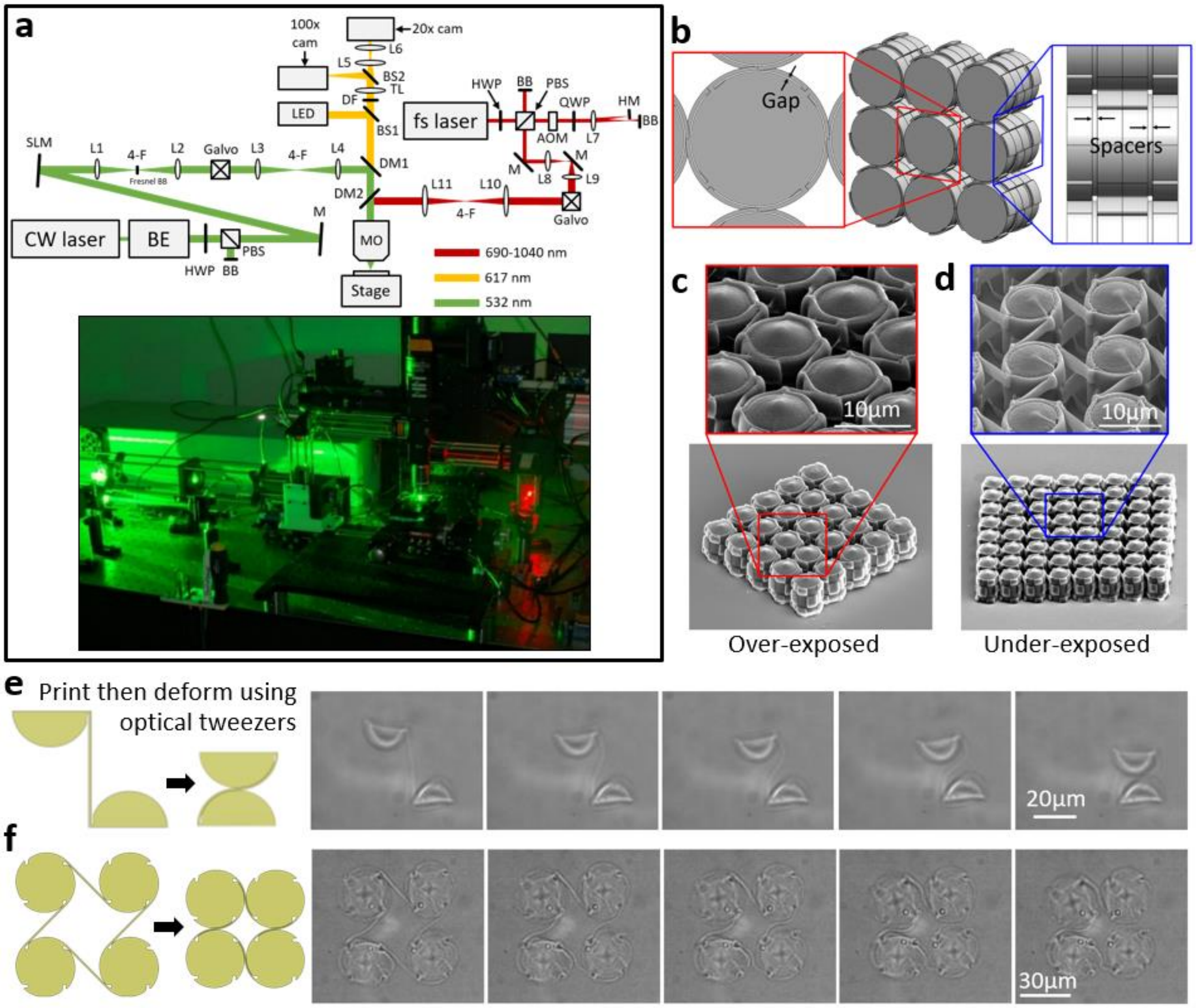

Figure 3.9 a. Our hybrid TPL/HOT system can be used to directly print lattices with already curled straps as long as gaps and spacers are added b. Such lattices have issues, however, when they are slightly over-exposed c. or under-exposed d. Our system can also use optical tweezers to deform the flexure straps after they have been printed straight to fabricate CRJs e. and CRAMs f. with stored strain energy so they can achieve their intended properties.

Acknowledgments

This work was supported by AFOSR under award number FA9550-15-1-0321, by Dr. Hopkins' DOE-nominated Presidential Early Career Award for Scientists and Engineers under award number B620630, and by the National Science Foundation Graduate Research Fellowship under

Grant No. DGE-1650604. The authors gratefully acknowledge program officer Byung “Les” Lee and thank Dr. John Fourkas and Dr. Farah Dawood for assistance in the preparation of the photopolymer and substrates.

Chapter 4. Automated Optical-tweezers Assembly of Engineered Microgranular Crystals

1. Granular Crystals

Microgranular crystals [74–76] have been a topic of much interest in recent years because of their potential to achieve unique and extreme mechanical behaviors. Similar to other kinds of granular media, [77–79] the closely packed spheres that constitute these crystals (Figure 4.1A) specifically give rise to unique stress-wave propagation behaviors due to the nonlinear Hertzian contact stiffness [80] between the spheres. Such stress-wave propagation behaviors, however, cannot be controlled unless the crystals are fabricated such that their constituent spheres can be arranged as desired (e.g., in highly ordered packing patterns that purposefully leverage the locations of void spaces). Figure 4.1A shows a graded crystal with a lattice that transitions between four differently packed lattice configurations.

The ability to fabricate engineered microgranular crystals with specifically placed spheres would enable numerous applications. Whereas macro-sized granular media consisting of >1 mm-sized spheres support stress-wave frequencies of Hz-kHz for audible acoustic applications such as sound scramblers [81], microgranular crystals consisting of nano- to micro-sized spheres can support stress-wave frequencies of MHz-GHz for higher-energy applications. Such applications include armor that mitigates or redirects shock waves caused by explosions or high-speed impacts, [82,83] fast responding mechanical logic elements, [84] switches and rectifiers, [85] and high-energy acoustic lenses [86,87] that focus high-frequency phonons for enabling nondestructive material-damage detection, [88] noninvasive surgery and medical imaging capabilities, [88] or advanced underwater imaging, sensing, and mapping [87]. Recent studies [87,89] demonstrate that the spatial resolution of propagating stress waves in a granular acoustic lens, and consequently the size of its achievable focal area, is limited by the size of the spheres that constitute the lens. Thus, the smaller the spheres that can be arranged within an acoustic lens, the smaller the achievable focal area. Additionally, sufficiently small spheres arranged within crystal lattices passively adhere to one another due to intermolecular forces and thus behave more like traditional homogenous materials that do not require impractical enclosures to hold their constituent components together like macro-sized spheres that require a container. Moreover, crystals with submicron-sized spheres

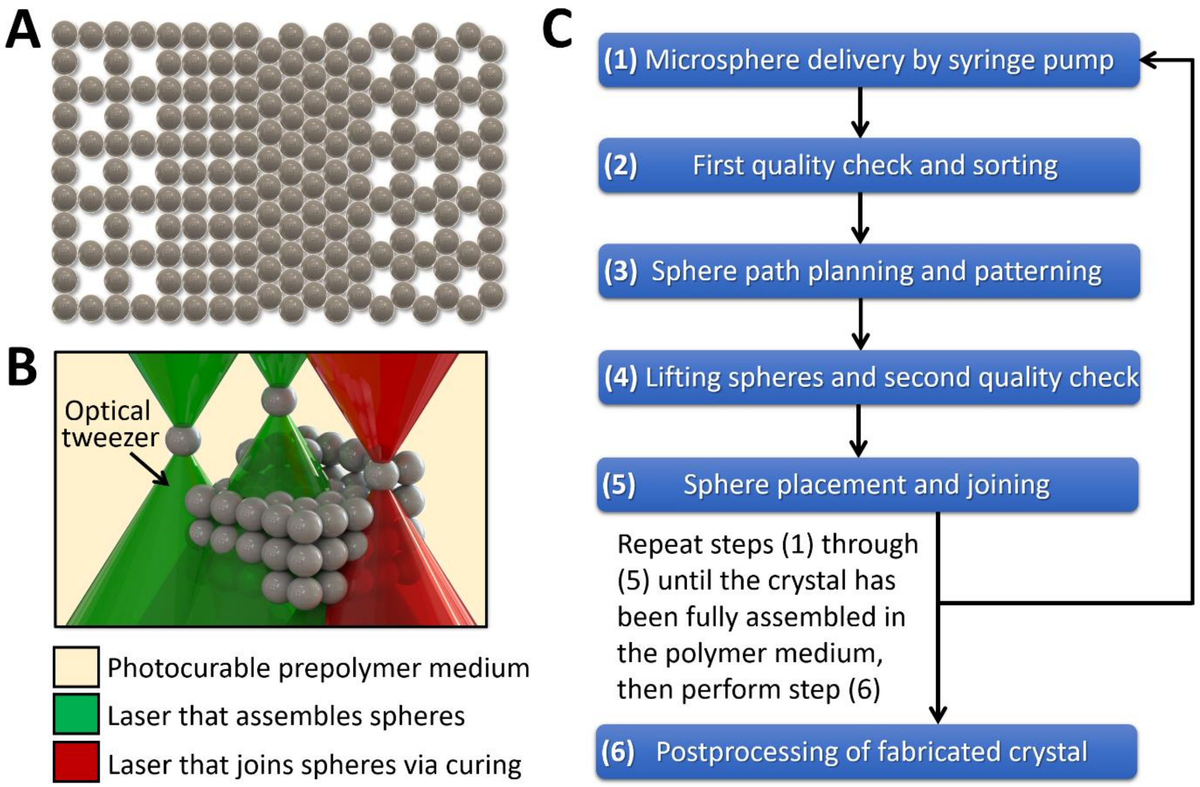

Figure 4.1 A) Two-dimensional granular crystal engineered with a graded lattice topology that alters its packing configuration across its geometry. B) The proposed fabrication approach uses optical tweezers to assemble microspheres within a photocurable pre-polymer medium that is cured by a femtosecond laser at select locations between the spheres to join them together. C) Steps of the automated approach created to fabricate three-dimensional engineered microgranular crystals.

can be engineered to control the propagation of electromagnetic waves for enabling photon-based applications. The behaviors of such photonic crystals have been found to be extremely sensitive to the packing order and imperfections in the relative positions of their nano-sized spheres [90–92].

Despite their tremendous potential, engineered granular crystals with specifically placed micro/nano-sized spheres are not yet practical technology primarily due to the fact that few approaches exist that can fabricate them. Although a variety of self-assembly [93–96] and electrophoretic deposition [97] approaches can fabricate some ordered 3D microgranular crystal designs, these approaches lack the flexibility necessary to fabricate general crystal configurations beyond a few varieties (e.g., hexagonal close-packed) or to position specific microspheres in specific locations within the crystal's lattice.

Optical-tweezers [98] have been proposed as an effective pick-and-place approach for solving this flexibility issue. Optical tweezers are focused laser beams that trap and hold macro/nano-sized particles near the waist of their focal point (Figure 4.1B) due to stabilizing forces created by electric-field gradients. By independently controlling the locations of these focal points (i.e., laser traps), microspheres can be moved and assembled to construct desired crystal lattices. The most impressive microgranular crystal fabricated using optical tweezers prior to this work, is a 3x3x3 cubically packed crystal that was manually assembled using a single optical trap, which individually assembled each of its 27 constituent microspheres one at a time [28]. Although this approach provides sufficient flexibility to fabricate general crystal designs, it is difficult to manually assemble crystals larger than a 3x3x3 lattice because manual assembly is impractically tedious and produces unacceptable stack-up errors due to human imprecision.

This paper introduces a fully automated approach that utilizes holographic optical tweezers [99] to assemble many microspheres simultaneously rapidly and with sufficiently high positioning accuracy (i.e., ~120 nm) to enable the fabrication of practical volumes of 3D engineered microgranular crystals of desired configurations. Holographic optical tweezers are generated by reflecting a single laser beam off of a spatial light modulator (SLM) that can actively change the phase of the beam's wavefront to generate multiple independently controlled optical tweezers (two are shown green in Figure 4.1B), which can be arranged as desired using principles of constructive and destructive interference. In the proposed approach, microspheres are suspended in a photocurable pre-polymer medium and are dispensed through a microfluidic device to the build site where the generated holographic optical tweezers (set to a wavelength that does not cure the pre-polymer medium) assemble the spheres simultaneously within the desired crystal lattice configuration. A femtosecond laser (set to a wavelength that does cure the pre-polymer medium) is focused (shown red in Figure 4.1B) at the regions between the spheres to permanently join them together once in place using cured spots of polymer 'glue'.

Although a variety of microsphere materials and sizes could be used with this approach, we used 4.86 μm-diameter silica microspheres from Bangs Laboratories to generate the results of this work. The spheres were surface-functionalized with carboxyl (COOH) groups to give them a negative charge for helping to prevent the spheres from clumping together or sticking to the substrate. The photocurable polymer medium in which these spheres were mixed consisted of 90.3 wt% deionized (DI) water as the solution's solvent, 9.5 wt% ethoxylated(15) trimethylolpropane tri-acrylate (Sartomer 9035) as the solution's monomer, 0.2 wt%, sodium 4-[2-(4-morpholino)benzoyl-2-dimethylamino] butylbenzenesulfonate (MBS) [100] as the solution's photoinitiator, and 0.025 wt% Tween 80 as the solution's surfactant. The solution was mostly water because it has a relatively low viscosity and a large index-of-refraction mismatch with silica compared to other pre-polymer chemistries. Thus, the solution enables the rapid handling of particles with large optical-trapping forces. It is important, however, that not too much water be used to dilute the solution; otherwise, the photopolymerization process will be inhibited. MBS was selected as the photoinitiator because it is water-soluble, initiates a two-photon polymerization reaction at 690 nm (i.e., the wavelength of our femtosecond laser), and possesses a low one-photon absorptivity at 532 nm (i.e., the wavelength of our optical-tweezers laser). The microspheres solution was allowed to sit for >12 hours to reduce the bubbles generated from mixing the Sartomer 9035 with the water.

The specific steps of the automated process for fabricating the engineered 3D microgranular crystals of this work using this microsphere-suspended photocurable pre-polymer solution are shown in Figure 4.1C and described in detail in what follows.

(1) Microsphere delivery by syringe pump: The first step in the process is to reliably deliver a steady stream of microspheres to the build site on demand. The photocurable pre-polymer medium, in which the microspheres are suspended, is pumped into a custom-made microfluidic device, which is depicted and described in detail in the experimental section, using a computer-controlled syringe pump. The microfluidic device's channel through which the medium is pumped consists of glass that is functionalized using (tridecafluoro-1,1,2,2-tetra-hydrooctyl) dimethylchlorosilane (Gelest) in an evacuated desiccator overnight to help prevent the microspheres from sticking to the channel's surfaces. The syringe pump dispenses the microsphere suspension medium at a rate of 500 μL/hr for two second intervals until microspheres are delivered to the region circumscribed by the orange box shown in Figure 4.2, which the system's camera monitors.

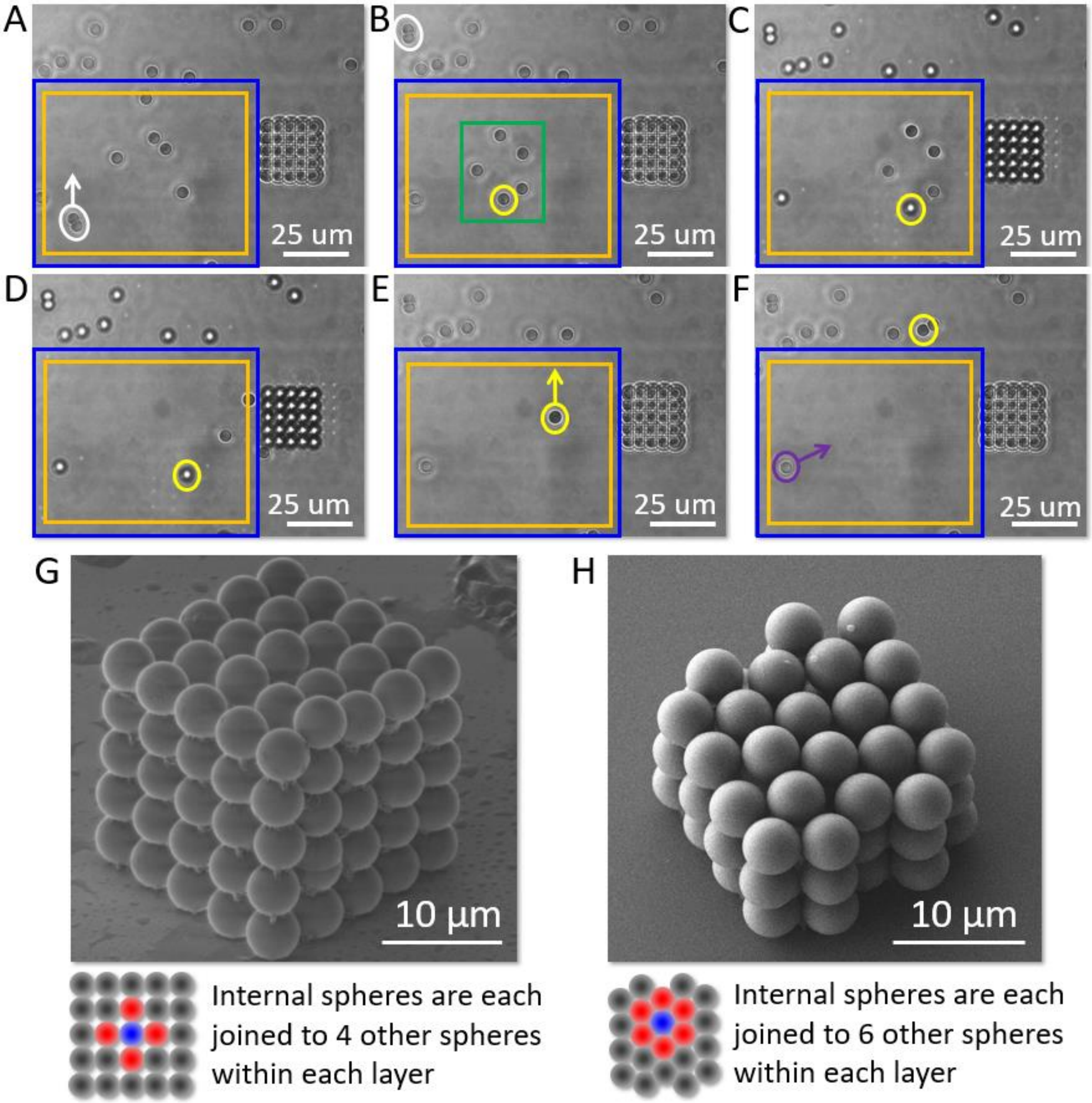

Figure 4.2 A) Spheres that are pumped to the build site are checked for quality, and if they are stuck together or are too large or small, they are disposed of. B) The spheres that pass the quality check are moved by optical tweezers to stable holding patterns that produce high-quality uniform-power optical traps. C) The spheres are then lifted as a second quality check to identify defective spheres that cannot be picked up by optical tweezers. D) The spheres that are picked up are moved to their final location within the crystal and are joined together using the femtosecond laser. E)

The spheres that could not be lifted are disposed of by optical tweezers. F) The algorithm then fills in any spheres that did not pass the second quality check. The process is repeated until microgranular crystals of any desired packing configuration are achieved. G) and H) show SEM images of differently packed crystals assembled using this approach.

(2) First quality check and sorting: Once microspheres are detected within both the blue and orange boxes shown in Figure 4.2A using image processing algorithms, the syringe pump stops the flow so that the spheres can be assessed for quality and then sorted. The algorithms used to detect the spheres perform a background subtraction step followed by a circular Hough transform [101]. Once detected, an algorithm identifies low-quality spheres with diameters that are outside an acceptable threshold (i.e., too large or too small), are not circular enough, or are inseparably clumped to other spheres like the pair shown inside the white circle of Figure 4.2A. The camera detects spheres in both the blue and orange boxes shown in the figure so that the algorithm does not mistakenly identify a sphere as acceptable if the sphere lies in the orange box but is clumped to other spheres that lie outside the orange box in the blue box. Optical tweezers are then used to move the low-quality spheres above the blue box where they are discarded. Other optical tweezers simultaneously trap the remaining spheres that passed the first quality check and hold them in place as the syringe pump again flows the pre-polymer medium for another two second interval. This process is repeated until enough high-quality spheres are trapped in the orange box that are equal or greater in number than the maximum number of spheres that the system is capable of simultaneously handling using optical tweezers. Details pertaining to the maximum number of spheres that our system can simultaneously handle (i.e., five silica spheres with 4.68 μm-diameters) as well as what limits that number for general systems are provided in Supporting Information.

(3) Sphere path planning and patterning: Once the sufficient number of spheres that pass the first quality check has been identified and optically trapped, a path planning algorithm is used in conjunction with closed-loop control to move the spheres to a stable holding pattern. A stable holding pattern constitutes a combination of sphere locations that, when populated by holographic optical tweezers, SLM produces uniform-power high-quality optical traps without also generating significant higher-order harmonic ghost traps [102]. The Gerchberg-Saxton phase retrieval algorithm [103], which is used to generate phase patterns on the SLM for generating holographic optical tweezers at desired locations, tends to produce low-quality non-uniform-power optical traps while also producing incidental unwanted traps (i.e., ghost traps) if the trap locations are ordered along a line. Thus, stable holding patterns, like the pattern shown inside the green box of Figure 4.2B, are best achieved when no more than two sphere locations lie along a common line. Additional discussion about stable holding patterns is provided in Supporting Information. Once a stable holding pattern is determined, a path planning algorithm assigns the initial locations of the optically trapped spheres that passed the first quality check (e.g., the location of the spheres in the orange box of Figure 4.2A that are not circled white) to the locations in the holding pattern (e.g., the location of the spheres in the green box of Figure 4.2B). To this end, the algorithm applies the linear assignment problem (LAP) [104], which is solved via the fast Hungarian algorithm [105] to identify the sphere assignment combination that produces the minimum total travel distance [106]. The collision-prevention algorithm detailed in Shaw *et al.* [106] is then used to move the spheres to the locations within the holding pattern using 11 mW optical tweezers for each sphere while ensuring that none of the spheres collide along the way. The visual feedback from the camera closes the loop on the control so that the spheres are guaranteed to arrive in their desired holding pattern.

(4) Lifting spheres and second quality check: After the spheres arrive in their desired holding pattern (Figure 4.2B), they are advanced forward while being held in that same pattern (Figure 4.2C) using optical tweezers. As they move, the system's piezoelectric microscope objective scanner raises the spheres off of the bottom of the substrate in a step-like sequence while the power supplied to each optical tweezer holding them is doubled (i.e., 22 mW per sphere). This doubling of power is supplied because it has been demonstrated that more power is required to lift a sphere than to move it in-plane using optical tweezers [53]. As the microscope objective scanner adjusts to lift the spheres, the spheres that remain on the substrate go out of focus and appear white in the center with a dark ring around their circumference (Figure 4.2C). Thus, image processing algorithms can leverage this observation to identify spheres that the optical tweezers fail to lift. Such spheres typically fail to be lifted if they are not sufficiently spherical, possess internal defects, or possess contaminants on their surface that interfere, obstruct, or absorb the incoming optical tweezer light. The sphere circled yellow in Figure 4.2 is an example of a sphere that failed to be lifted by our system due to imperfections. The spheres that pass this second quality check by successfully being lifted off the substrate are raised to a height that is one sphere radius above the spheres on the top layer of the crystal being fabricated to prevent collisions during assembly.

(5) Sphere placement and joining: Once the spheres that pass the second quality check are lifted by their optical tweezers, they are moved in a straight line directly to the location above where they will be placed in the crystal (Figure 4.2D). The algorithm ensures that no paths cross because closed-loop path planning is not possible during this step since the transparent spheres are not recognizable by the image processing algorithm once they are above the partially constructed crystal. Once in place, the spheres are lowered onto the crystal (or onto the substrate in the case of the first layer) using the microscope objective scanner. The algorithm then determines the contact points between the newly placed spheres and their surrounding spheres (and/or the substrate surface). The system's femtosecond laser is directed by a galvanometer to those locations so that the pre-polymer medium in the regions between the spheres (and/or the substrate) are cured to join them together, thus, holding the crystal firmly in place during the fabrication process. The laser imparts 30 mW of average power in 100 fs pulses with a wavelength of 690 nm over a duration of 180 ms during this joining process. An X-shaped pattern is scanned at these locations to improve sphere joining by accommodating lateral misalignment error between the system's optical-tweezers laser and femtosecond laser. More discussion on details of lasers alignment and calibration in our system are provided in the experimental section. After the spheres that passed the second quality check are arranged and joined within the crystal being fabricated, optical tweezers are used to move any spheres that failed the second quality check above the blue box to dispose of them (e.g., the sphere circled yellow in Figure 4.2E). Steps (1) through (5) are then repeated to fill any locations with high-quality spheres (e.g., the sphere circled purple in Figure 4.2F) that were intended to be assembled within the crystal but were not because of the second quality check. The entire process is then repeated until the full crystal is fabricated. It is worth noting that after each layer of spheres has been constructed in the crystal, a grid pattern of lines that pass through each sphere's central location within that layer is scanned using the femtosecond laser to further solidify each sphere in its place. Furthermore, less power is used to join spheres the higher up they are in the crystal because there is less medium to absorb the laser's power, the higher the laser is focused on the microfluidic device's channel. Thus, if the same power is used to join spheres at the top of the crystal as is used to join spheres at the bottom, the aqueous medium tends to boil and destroy the crystal's lattice.

(6) Post-processing of fabricated crystals: Once the crystal is fully fabricated, a post-processing procedure must be conducted to evacuate the surrounding photocurable pre-polymer medium and remove the crystal from its microfluidic device without damaging or deforming its lattice. To this end, DI water is pumped into the microfluidic device to flush out the uncured pre-polymer medium along with any unused or defective microspheres. The microfluidic device is then flushed with ethanol, which has low surface tension and evaporates quickly without deforming the crystal. Additionally, care must be taken to ensure that bubbles are not generated with each subsequent flush of the microfluidic device. Supporting Information provides further discussion pertaining to post-processing crystal damage. After the final ethanol flush, the coverslip on the microfluidic device is cut open using a diamond scribe, and the exposed sample is coated with a 10 nm layer of gold to enable scanning electron microscope (SEM) imaging.

SEM images of two differently packed silica crystals that were fabricated using the automated holographic-optical-tweezers approach introduced in this chapter are provided in Figure 4.2G and Figure 4.2H. The crystal shown in Figure 4.2G consists of almost five times more spheres than the previous record-large crystal that was manually assembled using optical tweezers [28]. The 3D crystal shown in Figure 4.2H possesses a packing structure that has never been fabricated previously using optical tweezers. Supporting Information of this thesis provides a sped up supplementary video of the crystal of Figure 4.2G being fabricated using the automated algorithm of this work, which took one hour to complete (Video 7). Note that the X-shaped polymer joints between the crystal's spheres are visible below each sphere in Figure 4.2G. Note also that these pervasive joints caused some unwanted stack-up errors in various columns within the crystal. The reason that these joints are much larger and less controlled than the side-by-side joints between neighboring columns of spheres is that each transparent sphere behaves like a lens that focuses the femtosecond laser further and thereby triggers more curing of the photocurable polymer medium directly below the sphere. Despite the stack-up errors present in the crystal of Figure 4.2G, the position accuracy of 265 nm and a precision (i.e., repeatability) of 155 nm were measured using the approach discussed in Supporting Information. By customizing the femtosecond laser's power for different kinds of joints (e.g., joints below or to the side of neighboring spheres) or by scanning differently shaped joints (e.g., O-shaped joints instead of X-shaped joints), higher quality crystals are expected. Validating this hypothesis and characterizing the effects of the resulting polymer joints on the mechanics of their crystals is a topic of future work. Additionally, we plan to adapt the presented automated approach to enable the fabrication of engineered crystals consisting of differently sized microspheres of different materials (e.g., a mixture of ceramic, polymer, and metal spheres).

Finally, note that after fabricating numerous copies of the crystals shown in Figure 4.2G and H, we have observed that the current automation approach succeeds in fabricating the crystals with negligible defects ~70% of the time. Light absorbing contaminates that cause localized boiling within the crystal and permanently joined beads that are not visibly distinct from single spheres because they arrive at the build site stacked out-of-plane are the most common causes of assembly failure. Improved fabrication success is anticipated as the assembly algorithms are refined and as the preparation quality of the pre-polymer medium is improved. In addition to the adjustments made to the joining approach discussed previously, it is also anticipated that these changes will also improve the positioning accuracy and repeatability of the assembly process.

2. Maximum achievable throughput estimation

We estimate that the maximum microgranular crystal throughput (i.e., the volume of crystal fabricated per hour) that an optical-tweezers system could achieve is 3.4 mm^3/hour. In this section, we provide the derivation for this estimate. We assume a typical holographic optical tweezers (HOT) system that uses standard Gaussian laser beams to handle transparent spherical microparticles.

In order to find the maximum throughput of the HOT approach, we first approximate the maximum speed, $v_{\mathrm{OT,max}}$, that each microsphere can be moved through its viscous medium using optical tweezers. Each colloidal microsphere experiences a total force, F_{total}, comprised of both internal and external forces according to

$$F_{\mathrm{total}} = F_{\mathrm{hydro}} + F_{\mathrm{Brownian}} + F_{\mathrm{DLVO}} + F_{\mathrm{OT}}. \tag{1}$$

The first three terms represent the internal forces that account for implicit solvent-colloid (F_{hydro}, F_{Brownian}) and colloid-colloid (F_{DLVO}) interactions. The last term (F_{OT}) is the external driving force due to the presence of a 3-dimensional optical field (i.e., optical trapping potential wells). The solvent model [107,108] implicitly incorporates dissipative lubrication forces $F_{\mathrm{hydro}}(\mathbf{r};\ \eta)$ and Brownian contributions $F_{\mathrm{Brownian}}(\mathbf{r};\ T\ )$ between nearby colloids at positions $\mathbf{r}$ in a continuum suspension with uniform viscosity η and temperature T. Steric, van der Waals, and electrostatic inter- colloidal forces $F_{\mathrm{DLVO}}(\mathbf{r};\ a,\ A_{\mathrm{col}},\ \lambda_D,\ A_{\mathrm{Yuk}})$ are treated within the Derjaguin-Landau-Verwey-Overbeek [109–111] (DLVO) framework. The former terms are modeled by a widely-used pairwise potential with characteristic size a and Hamaker constant A_{col} [112]. The latter term describes electrostatic repulsion between electric double layers formed by ions in the fluid that screen the surface charge of colloids over the characteristic Debye length λ_D. This also is modeled in a pairwise fashion with a variant of the Yukawa potential [113] with interaction constant A_{Yuk} that is set by the zeta-potential ζ, relative permittivity ϵ, ion valence q, and temperature T [114–116]. The external force that causes optical trapping $F_{\mathrm{OT}}(E; q_{\mathrm{col}})$ depends on the applied electric field E acting on a colloid with effective charge q_{col} [117]. As detailed by Ashkin [118], trapping efficiency, Q, represents the amount of momentum of the laser beam converted into trapping force per photon. This trapping efficiency has units of $n\hbar k$ per photon, where n is the refractive index of the particle, $\hbar$ is the Planck constant, and k is the wave vector. Q is also sensitive to parameters that describe the focused laser beam (i.e., laser quality M^2, numerical aperture NA, beam profile, and polarization) [119]. In general, Q is axisymmetric for a plane-polarized Gaussian laser beam and often expressed in terms of its axial (Q_z) and radial (Q_r) components. Q is converted into a force with conventional units by multiplying it by nP/c where P is the laser power at the trap plane and c is the speed of light in a vacuum; thus, $F_{OT}(r) = Q_r nP/c$ and $F_{OT}(z) = Q_z nP/c$. Experimental results [120–122] have confirmed that F_{OT} scales linearly with P. In the absence of hardware limitations (e.g., laser power, optical aberrations, and losses), P is limited by thermal effects (namely, the localized heating at the colloid-fluid interface) and the spatial light modulator (SLM) performance. The thermal effects are highly system-specific and vary greatly with the selection of material and media [123]. For the sake of brevity and the scope of this work, we will evaluate the laser power limit, based on the specifications of our hybrid experimental system (details in previous chapters and [124]), to be $P = 400$ mW at the trap plane. Using the model described in the work of Porter *et al.* [125], the maximum optical tweezing force, $F_{\mathrm{OT},max}$, is calculated to be $Q_{max} nP/c = 0.146 * 1.33 * 400\ mW * / 3e8\ m/s =$ 258.36 pN.

To predict the maximum continuous drag speed, $v_{OT,max}$, using a single optical tweezer, we consider the steady-state behavior of a single sphere in an optical trap that moves with respect to the medium at a constant velocity, v_{OT}. A trapped sphere follows a moving trap at a steady-state equilibrium lag distance determined by the balance of forces in Eq. 1. By considering the steady-state case, we can ignore the effects of F_{DLVO} and F_{Brownian} (whose time-averaged values are zero), and simplify Eq. 1 to

$$F_{\mathrm{OT}}(r_p - r_{OT}) - F_{hydro}(v_{OT}) = 0 \quad => \quad v_{OT,max} = F_{\mathrm{OT},max} / 6\pi\eta a. \qquad (2)$$

Thus, we can predict the maximum stable continuous drag speed using Eq. 2. By equating the calculated value of maximum optical trapping force ($F_{OT,max,}$=258.36 pN) to the Stokes drag force coefficient for a sphere ($6\pi\eta a = 6*\pi*8.9e\text{-}4\ N\ s/m\text{^}2*4\mu m = 6.71e\text{-}8\ N\ s/m$) in Eq. 2 and assuming a sphere diameter of 4 µm, we estimate that the maximum sphere velocity, $v_{OT,max}$, to be 3.85 mm/s.

The number of spheres that can be handled by the HOT approach depends on the maximum number of traps that can be generated by the SLM, which is limited in its resolution (i.e., hologram quality) and its damage threshold (i.e., the limit on the maximum laser power that can be distributed among the optical traps). An ideal SLM would be able to trap all spheres found in the field of view (FOV) of the microscope objective. The FOV is a set characteristic of objective lenses that is calculated based on magnification and field number of the lens. For the objective that was considered for calculations in the previous part, the FOV is 0.14 mm by 0.17 mm. This means that, in the case of 4 µm silica spheres, and usage of 80% of FOV (to allow for collision-less dynamic repositioning), a maximum of 1,178 spheres, n_{max}, can be handled simultaneously to form an edge-to-edge square packing (in an N-by-M array, where are estimated to be N=31 and M=38 based on the size of the FOV).

In order to fabricate large granular structures with HOT, the microspheres that are found in a single working area may not suffice. Therefore microparticle delivery system [126] is required to flow in spheres on demand. The rate of sphere delivery, r_{delivery} (spheres/s), is a product of the microfluidic flow rate, V_{flow} (µm/s), channel cross-sectional area, A (µm^2), and solid volume fraction of the solution, f_{sphere} (spheres/µm^3), and is given according to

$$r_{\text{delivery}} = V_{\text{flow}} \times A \times f_{\text{sphere}}. \tag{3}$$

By assuming reasonable values for microfluidic parameters of V_{flow}=100 µm/s, A=2x10^4 µm^2, f_{sphere}=0.025%, we calculate a rate of 500 spheres per second, which results in a time-averaged delivery period for each sphere (i.e., $t_{\text{delivery}}=1/r_{\text{delivery}}=1/500=2$ ms).

By considering an average sphere transport distance, d_{avg}, (i.e., the farthest a sphere may have to travel to be incorporated in the structure, which is approximately the corner to the center of FOV) was assumed to be 110 µm. However, this distance can likely be reduced with a proper choice of the path-planning algorithm [126]. Therefore, we find the transport time per sphere, $t_{transport}=d_{avg} / v_{OT,max}$, to be 28.6 ms.

In the final step, two-photon polymerization is employed to permanently join spheres together and to a substrate. We use an empirically-observed value (t_{cure}=50 ms) that accounts for curing time per sphere, including the time for galvanometer mirror-based laser steering. It follows that the time per sphere is the sum of these three-time values (i.e., $t_{delivery}+t_{transport}+t_{cure}$=80.6 ms). By considering the total number of spheres that can be handled at once (n_{max}=1,178), a 12.4 layered structure (volume per layer=7.4x10^{-5} mm^3) with 14,615 spheres can be built in a second, which results in a 3.37 mm^3/hr volumetric rate.

3. Experimental Details

3.1. Fabrication System

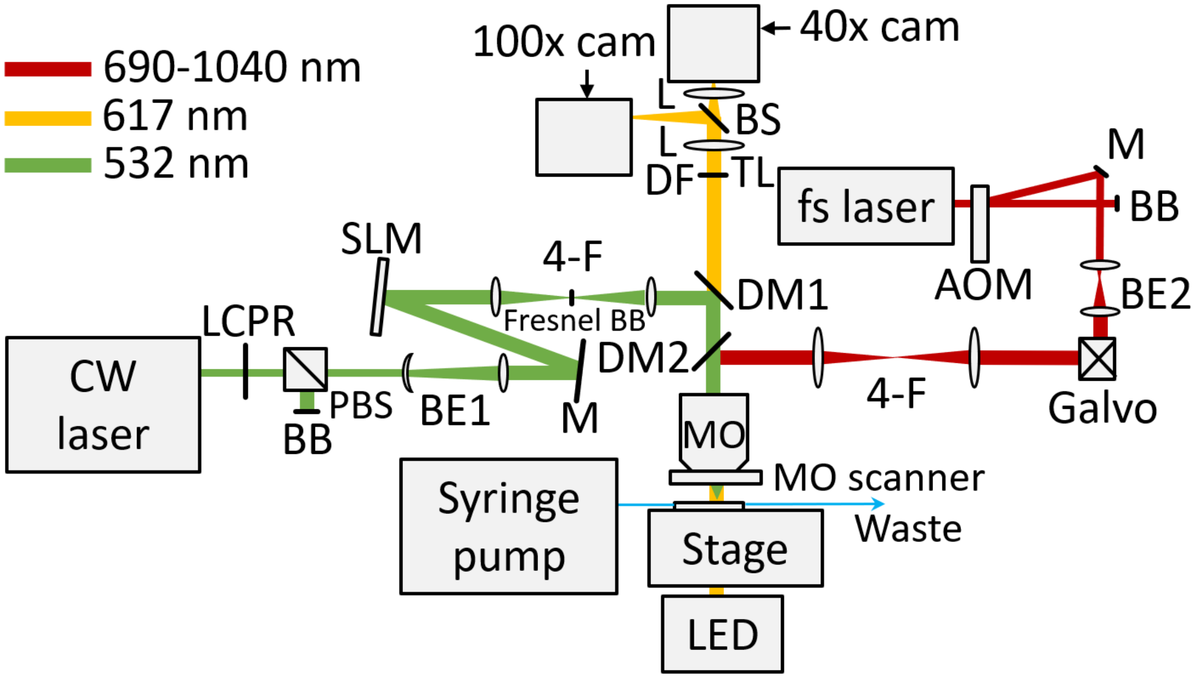

Figure 4.3 A schematic of the system used to fabricate microgranular crystals of any configuration.

The schematic of the system used to fabricate the crystals of Figure 4.2 is shown in Figure 4.3. The system consists of four main subsystems: (1) a microfluidic sphere delivery subsystem, (2) an imaging subsystem, (3) a holographic optical-tweezers subsystem, and (4) a two-photon polymerization subsystem. The microfluidic sphere delivery subsystem includes a Chemyx Fusion 100 syringe pump with a 1 mL syringe. Details pertaining to the components that constitute the custom-made microfluidic device are provided in Supporting Information. The imaging subsystem uses a 100x oil-immersion microscope objective (MO; Olympus Plan Apo Lambda, 1.45 NA) with a piezoelectric microscope objective scanner (MO scanner; Thorlabs PFM450E) and two cameras at 40x and 100x magnification (40x and 100x cam; Basler ace acA1300-75gm). The sample is illuminated by a light-emitting diode source (LED; Thorlabs M617L3) in a brightfield configuration. The other components in the imaging column include doublet lenses (L), beam-splitters (BS), a dichroic filter (DF), a tube lens (TL; Thorlabs ITL200), and dichroic mirrors (DM1 and DM2). The holographic optical-tweezers subsystem consists of a 532 nm continuous-wave laser (CW laser; Laser Quantum Opus 3W), a liquid crystal polarization rotator (LCPR; Meadowlark Optics LPR-100-0532), a phase-only spatial light modulator (SLM; Meadowlark Optics 1920 × 1152), a beam block (BB), a polarizing beam-splitter (PBS), a beam expander (BE1), a mirror (M), a 4-F telescope with a custom Fresnel beam block (Fresnel BB) at its focal plane relay, which consists of a 200-μm-diameter gold film deposited on a glass coverslip, and a short-pass dichroic mirror (DM1). The two-photon polymerization subsystem uses a tunable-wavelength femtosecond laser (fs laser; Spectra-Physics MaiTai eHP DS, 690-1040 nm), an acousto-optic modulator (AOM; IntraAction ATM-802DA2), scanning galvanometer mirrors (galvo; Thorlabs GVS012), a low-dispersion mirror (M), a beam block (BB), a beam expander system (BE2), 4-F telescope relay, and a long-pass dichroic mirror (DM2). The sample is mounted on a three-axis, stepper-motor-driven micro-positioning stage (Thorlabs RB13M, DRV001).

3.2. Microfluidic device details

This section details the microfluidic device used to fabricate the microgranular crystals. The microfluidic device (Figure 4.3A) was designed to deliver the microspheres to the build site. The flow velocity of the microsphere pre-polymer medium is significantly reduced as it transitions from the polyethylene micro-tubing (BD Intramedic) into the device's channel, which has a length of 4.5 cm length, a width of 2 cm width, and a depth of 70 μm. The low flow velocity is required to deliver manageable numbers of spheres to the build site and to stop the flow immediately on demand. The device is composed of two pieces of glass that sandwich a 70 μm-thick double-sided tape gasket as detailed in the exploded view of Figure 4.4B. The bottom piece of glass is a standard microscope slide, which is plasma cleaned and fluorinated to repel the carboxylated microspheres and prevent undesired sticking. The top cover glass is a Number 0 coverslip, which is shorter than the microscope slide. At each end, acrylic adaptors are glued in the opening using epoxy such that the tubing can be fitted to the device at the inlet and the outlet. Initially, the double-sided tape gasket was cut using a laser cutter, but we found that that process left a charred residue, so instead, the gaskets were cut by hand using a razor blade. It's important to note that the syringe pump should be placed above the microfluidic device during operation so that the silica microspheres, which due to their density, fall downward and thus do not get stuck in and clog the tubing.

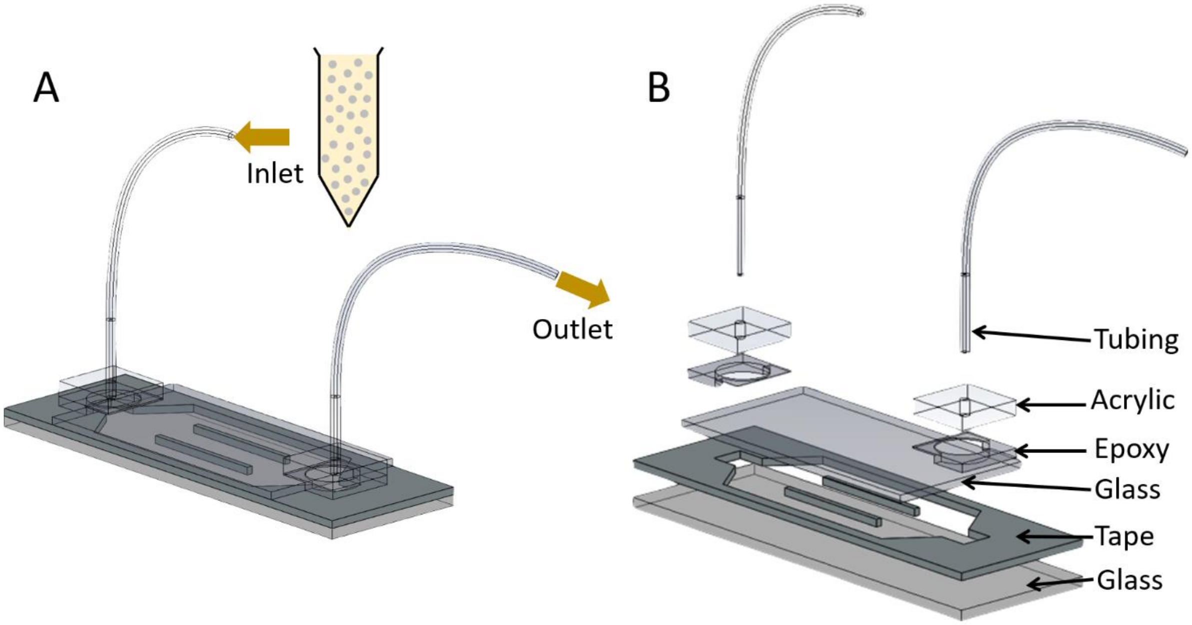

Figure 4.4 A) The microsphere-based photocurable polymer medium is pumped through our custom-made microfluidic device, which B) consists of multiple layered components.

3.3. Effects that govern the maximum number of spheres that can be simultaneously handled

The maximum number of microspheres that a general optical-tweezers system can simultaneously handle is affected by the size, sphericity, and material properties of the spheres as well as the optical, thermal, and hydrodynamic properties of the photocurable pre-polymer medium. Additionally, the maximum laser power that can be reflected off of the system's spatial light modulator (SLM) without damaging it and the quality of the optical traps that the system's SLM can produce also affect the maximum number of microspheres that a general optical-tweezers system can simultaneously handle.

It has been empirically observed from the author's optical-tweezers system that tens of 4.2 μm-diameter polystyrene microspheres can be simultaneously handled in a 2D plane [126], but only a maximum of five 4.86 μm-diameter silica microspheres can be simultaneously handled in 3D for the purposes of this work efforts due to the extra power per trap required for out-of-plane handing (i.e., along the axis of the laser beam) of larger and denser spheres [127].

3.4. Stable holding patterns

This section demonstrates why optical-tweezers holding patterns should not be arranged in a linear pattern. Simulation results (Figure 4.5) of the standard Gerchberg-Saxton (GS) phase retrieval algorithm indicates that the creation of optical traps in a linear configuration will result in a nonuniform distribution of optical-trap intensities at the trapping plane due to the creation of strong higher-order harmonics. For example, when a 1920×1152-pixel SLM generates five equally spaced traps along a line (as indicated by the red arrows in Figure 4.4A) using five iterations of the GS algorithm, the five traps exhibit dramatically different intensities. Additionally, unwanted "ghost" traps are generated that possess more intensity than some of the intended traps in the middle of the linear pattern. The lower intensity traps in the middle of this pattern are often insufficient to stably lift microspheres off of the substrate. Simply increasing the laser's power to compensate for this effect is not a desirable solution as an increase in power can initiate thermal polymerization and/or boiling of the pre-polymer medium at the locations of the higher intensity traps. To solve this issue, optical traps are arranged such that no more than two traps lie along the same line. Note from the pattern in Figure 4.5B, which is the same as shown in the green box of Figure 4.2B, that the same SLM simulation will produce a far more uniform intensity distribution with fewer and less consequential ghost traps than the linear pattern using the same algorithm. A detailed discussion of higher-order harmonic ghost traps produced using phase-only SLMs is provided in other works [102,128].

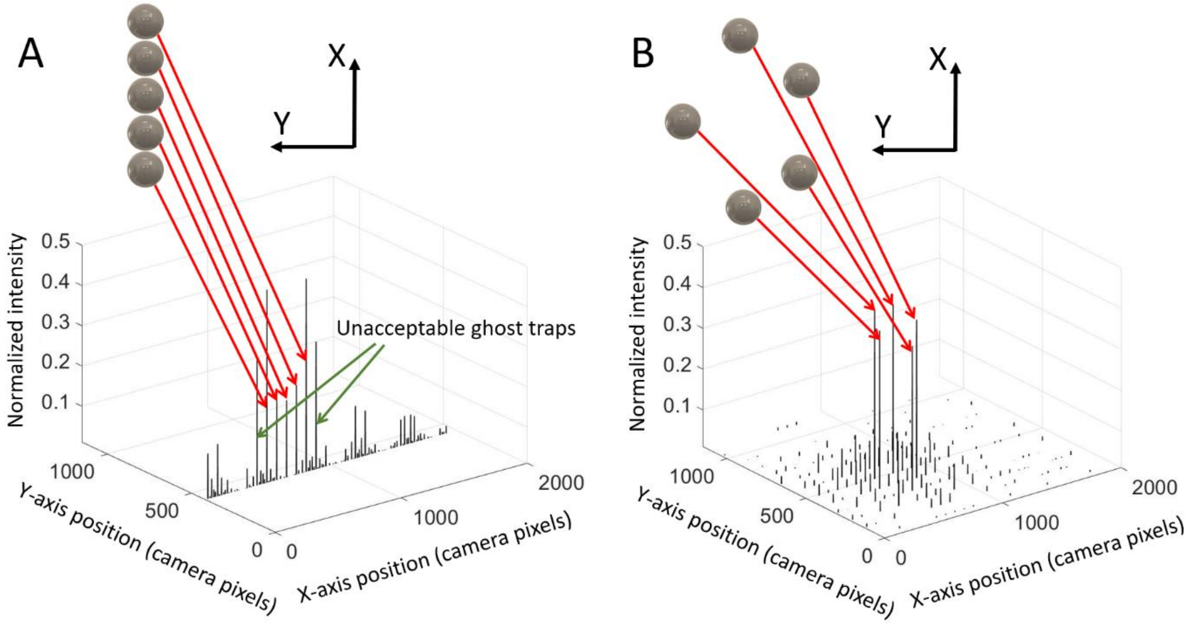

Figure 4.5 A) If the optical tweezers holding pattern is arranged along a straight line to stably trap microspheres in a row, the resulting traps will possess nonuniform power and be low quality, and there will be some unwanted ghost traps. B) If the holding pattern is arranged such that no

more than two of the spheres being trapped lie along a straight line, the resulting traps will possess uniform power and be of higher quality, and no significant ghost traps will be generated.

3.5. Aligning and calibrating the system's optical-tweezers laser and femtosecond laser

To achieve high precision and accuracy in the proposed microgranular crystal fabrication process, both the optical-tweezers handling laser and the femtosecond joining laser needs to be aligned and calibrated.

Full optical system alignment is performed by assuring that both the handling and joining laser beams hit the center of the system's mirrors and pass through the center of every lens in the optical path. If the handling laser is not aligned, the optical trap quality is reduced and becomes nonuniform across the trapping plane, which yields distorted crystal packings. If the joining laser is not aligned, higher laser power is needed for the photopolymerization process, which can induce thermal polymerization of the pre-polymer medium. Furthermore, the system's achievable polymerization voxel, which is the smallest volume that it can be polymerized, becomes larger (i.e., the system's resolution is degraded).

Calibrating both lasers is also an essential step in the fabrication process since it is critical that the automation algorithm accurately recognizes where the lasers' true position is in the trapping plane at any given moment. If the handling laser is not properly calibrated, it interferes with or even terminates the fabrication algorithm. If the joining laser is not properly calibrated, partial optical tweezing forces resulting from its focused beam dislocate the microspheres from the handling laser's optical traps that hold the spheres in place. Thus, improper calibration can cause the fabrication of warped crystal lattices. The handling laser is calibrated by trapping a microsphere and then using image processing to determine the coordinates of its center in the camera view.

These coordinates are then compared to the coordinates that were originally used by the SLM to generate the optical trap. The code then updates the correlation factor between the SLM and camera coordinates to ensure optimal accuracy within the automation process. A similar process is followed to calibrate the joining laser by using five polymerized spots distributed over the system's viewing area.

3.6. **Crystal damage caused by post-processing**

This section discusses lessons learned about preserving the lattice structure of a crystal during post-processing. Removing fabricated crystals from their microfluidic device and drying them is the process step that causes the most damage to the final crystal lattices. Water has a high surface energy and therefore produces strong capillary forces, which can easily warp and destroy the crystals. A solvent exchange from pre-polymer solution to water and then from water to ethanol is employed to reduce surface tension and improve the likelihood that the crystal will survive post-processing. Any bubbles that are produced in the microfluidic device's tubing or channel during this solvent exchange can prematurely expose the sample to unwanted capillary forces, which can destroy the crystal. Figure 4.5 shows how crystals can be warped and destroyed by capillary forces if the wrong combinations of solvents are used for flushing the microfluidic device (i.e., if air is used to evacuate the water within the device).

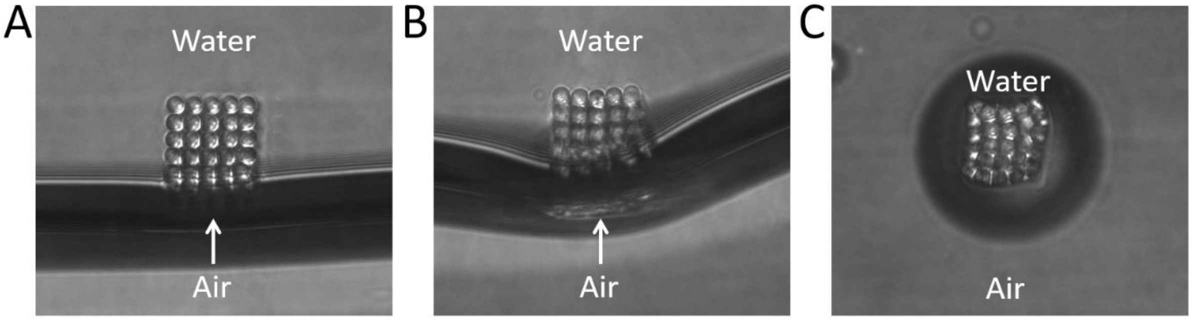

Figure 4.6 A) When air is used to evacuate water in the microfluidic channel, B) a surface tension tidal wave sweeps across the crystal, and C) deforms the lattice.

3.7. Accuracy and Precision Measurements

We measured the accuracy and precision (i.e., repeatability) of the sphere positions within the 5x5x5 crystal of Figure 4.2G after post-processing to be 265 nm and 155 nm, respectively. This measurement was achieved by performing image processing in MATLAB on a side-view SEM image of the crystal (Figure 4.7A). First, Hough transform [101] is implemented to detect the microspheres in the image as indicated by the blue circles in Figure 4.6. Then the distances from their center coordinates to their intended locations as indicated by the red circles shown in the same figure are averaged and reported as accuracy; the standard deviation of these distances is reported as precision.

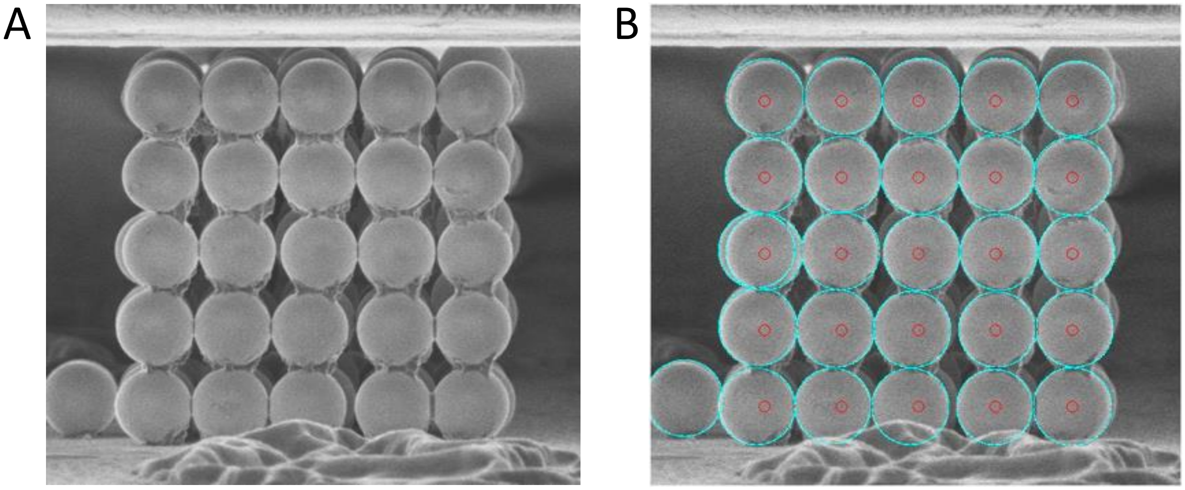

Figure 4.7 A) Side-view SEM image of the 5x5x5 crystal of Figure 2G. B) Spheres detected with image processing indicated with blue circles and intended sphere locations indicated with red circles.

Acknowledgments

The following researchers are acknowledged: Mr. Amin Farzaneh for assistance with the automation code, Mr. Michael Porter for assistance calculating the throughput of crystals, Dr. John Fourkas for providing the MBS photoinitiator, Dr. Farah Dawood for discussions regarding the preparation of the photopolymer and substrates, and Dr. Carlos Portola for constructive conversations.

Chapter 5. Conclusions

This thesis communicated advances in microfabrication capabilities of two-photon lithography (TPL) enabled by integrating microfluidics (MF) and optical tweezers (OT) into a custom-developed TPL system.

Chapter 2 demonstrated the fabrication of high-resolution multi-functional 3D cell carrier microparticles by bringing new capabilities to STP-CFL. Out-of-plane features can now be created with good fidelity without sacrificing the speed of fabrication. The future steps of this work include studying the self-alignment behavior of the fabricated microparticles, implementing cell adhesive material in the shelter region, loading cells on the carriers, and performing flow cytometry for downstream cell studies. More generally, we envision the STP-CFL system as an approach to rapidly prototype and analyze complex multi-material particles not only for bioengineering applications but also for use in studying novel particle-particle interactions in additive manufacturing and self-assembly.

Chapter 3 demonstrated the first integrated TPL and holographic OT system, capable of fabricating microstructures with embedded strain energy. The system can simultaneously print, deform, orient, displace, join, and actuate arbitrarily shaped free-floating bodies as desired. We advanced an open-source simulation tool to determine the optimal placement of optical traps for most efficiently handling such bodies. The simulation results indicated that optical traps are most efficient when they are positioned at the edges of bodies and slightly above their mid-plane. Informed by the results of the simulation tool, multiple polymer microsystems were fabricated in a photopolymer resin specifically developed for decoupled TPL-based printing and HOT-based handling.

Chapter 4 introduced the first-ever automated approach for fabricating engineered microgranular crystals using holographic optical tweezers combined with two-photon polymerization. The approach is the only existing way to fabricate such crystals of desired packing configurations. Moreover, it provides the only viable path toward fabricating practical volumes of such crystals in reasonable build times and with sufficient positioning accuracy to enable the field's long-sought stress-wave propagation applications. Although the automated approach demonstrated here achieved a significant increase in the number of spheres that are possible to assemble using optical tweezers as well as the speed with which they can be assembled, the current throughput of our automated system is only ~$14\text{x}10^{-6}$ mm^3 of crystal fabricated per hour. We estimate, however, that replacing our existing liquid-crystal-based SLM with a state-of-the-art micro-mirror array [129,130] could enable our approach to produce a throughput of as much as 3.7 mm^3 of crystal fabricated per hour. Such a throughput would enable practical sizes of engineered microgranular crystals for advanced applications.

Chapter 6. References

1. L. Li and J. T. Fourkas, "Multiphoton polymerization," Mater. Today **10**(6), 30–37 (2007).
2. T. Bückmann, N. Stenger, M. Kadic, J. Kaschke, A. Frölich, T. Kennerknecht, C. Eberl, M. Thiel, and M. Wegener, "Tailored 3D Mechanical Metamaterials Made by Dip-in Direct-Laser-Writing Optical Lithography," Adv. Mater. **24**(20), 2710–2714 (2012).
3. A. Vyatskikh, S. Delalande, A. Kudo, X. Zhang, C. M. Portela, and J. R. Greer, "Additive manufacturing of 3D nano-architected metals," Nat. Commun. **9**(1), 593 (2018).
4. L. R. Meza, S. Das, and J. R. Greer, "Strong, lightweight, and recoverable three-dimensional ceramic nanolattices.," Science **345**(6202), 1322–6 (2014).
5. D. Y. Kim, S. H. Jin, S. G. Jeong, B. Lee, K. K. Kang, and C. S. Lee, "Microfluidic preparation of monodisperse polymeric microspheres coated with silica nanoparticles," Sci. Rep. **8**(1), 1–11 (2018).
6. D. Dendukuri, K. Tsoi, T. A. Hatton, and P. S. Doyle, "Controlled synthesis of nonspherical microparticles using microfluidics," Langmuir **21**(6), 2113–2116 (2005).
7. M. Seo, Z. Nie, S. Xu, M. Mok, P. C. Lewis, R. Graham, and E. Kumacheva, "Continuous microfluidic reactors for polymer particles," Langmuir **21**(25), 11614–11622 (2005).
8. D. Dendukuri, D. C. Pregibon, J. Collins, T. A. Hatton, and P. S. Doyle, "Continuous-flow lithography for high-throughput microparticle synthesis," Nat. Mater. **5**(5), 365–369 (2006).
9. D. Dendukuri, S. S. Gu, D. C. Pregibon, T. A. Hatton, and P. S. Doyle, "Stop-flow lithography in a microfluidic device," Lab Chip **7**(7), 818–828 (2007).
10. N. Hakimi, S. S. H. Tsai, C.-H. Cheng, and D. K. Hwang, "One-Step Two-Dimensional Microfluidics-Based Synthesis of Three-Dimensional Particles," Adv. Mater. **26**(9), 1393–1398 (2014).

11. K. W. Bong, D. C. Pregibon, and P. S. Doyle, "Lock release lithography for 3D and composite microparticles," Lab Chip **9**(7), 863–866 (2009).

12. S. A. Lee, S. E. Chung, W. Park, S. H. Lee, and S. Kwon, "Three-dimensional fabrication of heterogeneous microstructures using soft membrane deformation and optofluidic maskless lithography," Lab Chip **9**(12), 1670–1675 (2009).

13. S. Habasaki, W. C. Lee, S. Yoshida, and S. Takeuchi, "Vertical Flow Lithography for Fabrication of 3D Anisotropic Particles," Small **11**(48), 6391–6396 (2015).

14. J. Lölsberg, A. Cinar, D. Felder, G. Linz, S. Djeljadini, and M. Wessling, "Two-Photon Vertical-Flow Lithography for Microtube Synthesis," Small **15**(33), 1901356 (2019).

15. C.-Y. Wu, K. Owsley, and D. Di Carlo, "Rapid Software-Based Design and Optical Transient Liquid Molding of Microparticles," Adv. Mater. **27**(48), 7970–7978 (2015).

16. D. Stoecklein, M. Davies, J. M. De Rutte, C. Y. Wu, D. Di Carlo, and B. Ganapathysubramanian, "FlowSculpt: Software for efficient design of inertial flow sculpting devices," Lab Chip **19**(19), 3277–3291 (2019).

17. S. C. Laza, M. Polo, A. A. R. Neves, R. Cingolani, A. Camposeo, and D. Pisignano, "Two-Photon Continuous Flow Lithography," Adv. Mater. **24**(10), 1304–1308 (2012).

18. A. Ashkin, J. M. Dziedzic, J. E. Bjorkholm, and S. Chu, "Observation of a single-beam gradient force optical trap for dielectric particles," Opt. Lett. **11**(5), 288 (1986).

19. K. C. Neuman and S. M. Block, "Optical trapping," Rev. Sci. Instrum. **75**(9), 2787–2809 (2004).

20. L. A. Shaw, S. Chizari, R. M. Panas, M. Shusteff, C. M. Spadaccini, and J. B. Hopkins, "Holographic optical assembly and photopolymerized joining of planar microspheres," Opt. Lett. **41**(15), 3571 (2016).

21. G. R. Kirkham, E. Britchford, T. Upton, J. Ware, G. M. Gibson, Y. Devaud, M. Ehrbar, M. Padgett, S. Allen, L. D. Buttery, and K. Shakesheff, "Precision Assembly of Complex Cellular Microenvironments using Holographic Optical Tweezers," Sci. Rep. **5**(1), 8577 (2015).

22. J. E. Curtis, B. A. Koss, and D. G. Grier, "Dynamic holographic optical tweezers," Opt. Commun. **207**(1–6), 169–175 (2002).

23. J. Köhler, Y. Kutlu, G. Zyla, S. I. Ksouri, C. Esen, E. L. Gurevich, and A. Ostendorf, "Optical assembly of microsnap-fits fabricated by two-photon polymerization," Opt. Eng. **56**(10), 1 (2017).

24. J. Köhler, S. I. Ksouri, C. Esen, and A. Ostendorf, "Optical screw-wrench for microassembly," Microsystems Nanoeng. **3**, 16083 (2017).

25. S. I. Ksouri, A. Aumann, R. Ghadiri, and A. Ostendorf, "Optical micro-assembling of non-spherical particles," in J. Glückstad, D. L. Andrews, and E. J. Galvez, eds. (International Society for Optics and Photonics, 2013), **8637**, p. 86370Z.

26. D. Palima and J. Glückstad, "Gearing up for optical microrobotics: micromanipulation and actuation of synthetic microstructures by optical forces," Laser Photon. Rev. **7**(4), 478–494 (2013).

27. M. J. Villangca, D. Palima, A. R. Banas, and J. Gluckstad, "Light-driven micro-tool equipped with a syringe function," Light Sci Appl. **5**(9), e16148 (2016).

28. F. Dawood, S. Qin, L. Li, E. Y. Lin, and J. T. Fourkas, "Simultaneous microscale optical manipulation, fabrication and immobilisation in aqueous media," Ch emical Sci. **3**(8), 2449 (2012).

29. M. Askari, "Metamaterial fabrication using combined multiphoton polymerization and

optical trapping," University of Nottingham (2017).

30. C. Y. Wu, D. Stoecklein, A. Kommajosula, J. Lin, K. Owsley, B. Ganapathysubramanian, and D. Di Carlo, "Shaped 3D microcarriers for adherent cell culture and analysis," Microsystems Nanoeng. **4**(1), 1–9 (2018).

31. L. N. Kim, S. E. Choi, J. Kim, H. Kim, and S. Kwon, "Single exposure fabrication and manipulation of 3D hydrogel cell microcarriers," Lab Chip **11**(1), 48–51 (2011).

32. J. Ahn, J. Ko, S. Lee, J. Yu, Y. T. Kim, and N. L. Jeon, "Microfluidics in nanoparticle drug delivery; From synthesis to pre-clinical screening," Adv. Drug Deliv. Rev. **128**, 29–53 (2018).

33. X. Zhu, C. Vo, M. Taylor, and B. R. Smith, "Non-spherical micro- and nanoparticles in nanomedicine," Mater. Horizons **6**(6), 1094–1121 (2019).

34. J. A. Champion, Y. K. Katare, and S. Mitragotri, "Particle shape: A new design parameter for micro- and nanoscale drug delivery carriers," J. Control. Release **121**(1–2), 3–9 (2007).

35. S. C. Glotzer, M. J. Solomon, and N. A. Kotov, "Self-assembly: From nanoscale to microscale colloids," AIChE J. **50**(12), 2978–2985 (2004).

36. S. C. Glotzer and M. J. Solomon, "Anisotropy of building blocks and their assembly into complex structures," Nat. Mater. **6**(8), 557–562 (2007).

37. H. Lee, J. Kim, H. Kim, J. Kim, and S. Kwon, "Colour-barcoded magnetic microparticles for multiplexed bioassays," Nat. Mater. **9**(9), 745–749 (2010).

38. S. C. Chapin, D. C. Appleyard, D. C. Pregibon, and P. S. Doyle, "Rapid microRNA Profiling on Encoded Gel Microparticles," Angew. Chemie Int. Ed. **50**(10), 2289–2293 (2011).

39. J. Lee, P. W. Bisso, R. L. Srinivas, J. J. Kim, A. J. Swiston, and P. S. Doyle, "Universal process-inert encoding architecture for polymer microparticles," Nat. Mater. **13**(5), 524–

529 (2014).

40. S. Han, H. J. Bae, J. Kim, S. Shin, S.-E. Choi, S. H. Lee, S. Kwon, and W. Park, "Lithographically Encoded Polymer Microtaggant Using High-Capacity and Error-Correctable QR Code for Anti-Counterfeiting of Drugs," Adv. Mater. **24**(44), 5924–5929 (2012).

41. N. Nitta, T. Sugimura, A. Isozaki, H. Mikami, K. Hiraki, S. Sakuma, T. Iino, F. Arai, T. Endo, Y. Fujiwaki, H. Fukuzawa, M. Hase, T. Hayakawa, K. Hiramatsu, Y. Hoshino, M. Inaba, T. Ito, H. Karakawa, Y. Kasai, K. Koizumi, S. W. Lee, C. Lei, M. Li, T. Maeno, S. Matsusaka, D. Murakami, A. Nakagawa, Y. Oguchi, M. Oikawa, T. Ota, K. Shiba, H. Shintaku, Y. Shirasaki, K. Suga, Y. Suzuki, N. Suzuki, Y. Tanaka, H. Tezuka, C. Toyokawa, Y. Yalikun, M. Yamada, M. Yamagishi, T. Yamano, A. Yasumoto, Y. Yatomi, M. Yazawa, D. Di Carlo, Y. Hosokawa, S. Uemura, Y. Ozeki, and K. Goda, "Intelligent Image-Activated Cell Sorting," Cell **175**(1), 266-276.e13 (2018).

42. K. Je, J. H. Kim, T. S. Shim, M. Ku, J. Yang, and S.-H. Kim, "Lithographically Designed Conical Microcarriers for Programed Release of Multiple Actives," Adv. Mater. Interfaces **5**(1), 1701163 (2018).

43. D. S. Kohane, "Microparticles and nanoparticles for drug delivery," Biotechnol. Bioeng. **96**(2), 203–209 (2007).

44. L. A. Shaw, S. Chizari, M. Shusteff, H. Naghsh-Nilchi, D. Di Carlo, and J. B. Hopkins, "Scanning two-photon continuous flow lithography for synthesis of high-resolution 3D microparticles," Opt. Express **26**(10), 13543 (2018).

45. W. E. Uspal, H. Burak Eral, and P. S. Doyle, "Engineering particle trajectories in microfluidic flows using particle shape," Nat. Commun. **4**(1), 1–9 (2013).

46. W. E. Uspal and P. S. Doyle, "Self-organizing microfluidic crystals," Soft Matter **10**(28), 5177–5191 (2014).

47. X. Zhou, Y. Hou, and J. Lin, "A review on the processing accuracy of two-photon polymerization," AIP Adv. **5**(3), 030701 (2015).

48. C. B. Churchill, D. W. Shahan, S. P. Smith, A. C. Keefe, and G. P. McKnight, "Dynamically variable negative stiffness structures," Sci. Adv. **2**(2), e1500778–e1500778 (2016).

49. N. Hu and R. Burgueño, "Buckling-induced smart applications: recent advances and trends," Smart Mater. Struct. **24**(6), 063001 (2015).

50. B. J. Hansen, C. J. Carron, B. D. Jensen, A. R. Hawkins, and S. M. Schultz, "Plastic latching accelerometer based on bistable compliant mechanisms," Smart Mater. Struct. **16**(5), 1967–1972 (2007).

51. S. Chu, J. E. Bjorkholm, A. Ashkin, and A. Cable, "Experimental Observation of Optically Trapped Atoms," Phys. Rev. Lett. **57**(3), 314–317 (1986).

52. T. A. Nieminen, H. Rubinsztein-Dunlop, and N. R. Heckenberg, "Calculation and optical measurement of laser trapping forces on non-spherical particles," J. Quant. Spectrosc. Radiat. Transf. **70**(4–6), 627–637 (2001).

53. T. A. Nieminen, V. L. Y. Loke, A. B. Stilgoe, G. Knöner, A. M. Brańczyk, N. R. Heckenberg, and H. Rubinsztein-Dunlop, "Optical tweezers computational toolbox," J. Opt. A Pure Appl. Opt. **9**(8), S196–S203 (2007).

54. D. B. Phillips, M. J. Padgett, S. Hanna, Y.-L. D. Ho, D. M. Carberry, M. J. Miles, and S. H. Simpson, "Shape-induced force fields in optical trapping," Nat. Photonics **8**(5), 400–405 (2014).

55. A. Callegari, M. Mijalkov, A. B. Gököz, and G. Volpe, "Computational toolbox for optical

tweezers in geometrical optics," J. Opt. Soc. Am. B **32**(5), B11 (2015).

56. G. A. Swartzlander, T. J. Peterson, A. B. Artusio-Glimpse, and A. D. Raisanen, "Stable optical lift," Nat. Photonics **5**(1), 48–51 (2010).

57. J. Liu, C. Zhang, Y. Zong, H. Guo, and Z.-Y. Li, "Ray-optics model for optical force and torque on a spherical metal-coated Janus microparticle," Photonics Res. **3**(5), 265 (2015).

58. P. Galajda and P. Ormos, "Complex micromachines produced and driven by light," Cit. Appl. Phys. Lett **78**, 249 (2001).

59. P. Galajda and P. Ormos, "Orientation of flat particles in optical tweezers by linearly polarized light," Opt. Express **11**(5), 446 (2003).

60. P. Jones, O. Maragò, and G. Volpe, *Optical Tweezers: Principles and Applications* (Cambridge University Press, 2015).

61. L. A. Shaw, S. Chizari, M. Dotson, Y. Song, and J. B. Hopkins, "Compliant Rolling-contact Architected Materials for Shape Reconfigurability," Nat. Commun. (2018).

62. S. Krödel, L. Li, A. Constantinescu, and C. Daraio, "Stress relaxation in polymeric microlattice materials," Mater. Des. **130**, 433–441 (2017).

63. S. Ushiba, K. Masui, N. Taguchi, T. Hamano, S. Kawata, and S. Shoji, "Size dependent nanomechanics of coil spring shaped polymer nanowires," Sci. Rep. **5**(1), 17152 (2015).

64. S. Nakanishi, S. Shoji, S. Kawata, and H. B. Sun, "Giant elasticity of photopolymer nanowires," Appl. Phys. Lett. **91**(6), 10–13 (2007).

65. R. S. Lakes, "Negative-Poisson's-Ratio Materials: Auxetic Solids," Annu. Rev. Mater. Res. **47**(1), 63–81 (2017).

66. K. E. Evans and A. Alderson, "Auxetic Materials: Functional Materials and Structures from Lateral Thinking!," Adv. Mater. **12**(9), 617–628 (2000).

67. A. Alderson and K. L. Alderson, "Auxetic materials," Proc. Inst. Mech. Eng. Part G J. Aerosp. Eng. **221**(4), 565–575 (2007).

68. M. Sanami, N. Ravirala, K. Alderson, and A. Alderson, "Auxetic Materials for Sports Applications," Procedia Eng. **72**, 453–458 (2014).

69. J. H. Reif, "Mechanical Computing: The Computational Complexity of Physical Devices," in *Computational Complexity* (Springer New York, 2012), pp. 1821–1836.

70. M. L. Roukes, "Mechanical compution, redux?," in *IEDM Technical Digest. IEEE International Electron Devices Meeting, 2004.* (IEEE, 2004), pp. 539–542.

71. X. Zheng, W. Smith, J. Jackson, B. Moran, H. Cui, D. Chen, J. Ye, N. Fang, N. Rodriguez, T. Weisgraber, and C. M. Spadaccini, "Multiscale metallic metamaterials," Nat. Mater. **15**(10), 1100–1106 (2016).

72. S.-H. Park, D.-Y. Yang, and K.-S. Lee, "Two-photon stereolithography for realizing ultraprecise three-dimensional nano/microdevices," Laser Photonics Rev. **3**(1–2), 1–11 (2009).

73. D. G. Grier, "A revolution in optical manipulation," Nature **424**(6950), 810–816 (2003).

74. N. Boechler, J. K. Eliason, A. Kumar, A. A. Maznev, K. A. Nelson, and N. Fang, "Interaction of a Contact Resonance of Microspheres with Surface Acoustic Waves," Phys. Rev. Lett. **111**(3), 036103 (2013).

75. S. P. Wallen, A. A. Maznev, and N. Boechler, "Dynamics of a monolayer of microspheres on an elastic substrate," Phys. Rev. B **92**(17), 174303 (2015).

76. N. Boechler, "Dynamics of Microscale Granular Crystals," in (Springer, Cham, 2017), pp. 73–77.

77. J. Duran, *Sands, Powders, and Grains: An Introduction to the Physics of Granular*

Materials (Springer Science & Business Media, 2012).

78. V. F. Nesterenko, "Propagation of nonlinear compression pulses in granular media," J. Appl. Mech. Tech. Phys. **24**(5), 733–743 (1983).

79. R. Nedderman, *Statics and Kinematics of Granular Materials* (Cambridge University Press, 2005).

80. K. Walton, "The effective elastic moduli of a random packing of spheres," J. Mech. Phys. Solids **35**(2), 213–226 (1987).

81. C. Daraio, V. F. Nesterenko, E. B. Herbold, and S. Jin, "Strongly nonlinear waves in a chain of Teflon beads," Phys. Rev. E - Stat. Nonlinear, Soft Matter Phys. **72**(1), (2005).

82. S. Sen, F. S. Manciu, and M. Manciu, "Thermalizing an impulse," Phys. A Stat. Mech. its Appl. **299**(3–4), 551–558 (2001).

83. F. Fraternali, M. A. Porter, and C. Daraio, "Optimal Design of Composite Granular Protectors," Mech. Adv. Mater. Struct. **17**(1), 1–19 (2009).

84. F. Li, P. Anzel, J. Yang, P. G. Kevrekidis, and C. Daraio, "Granular acoustic switches and logic elements," Nat. Commun. **5**(1), 5311 (2014).

85. N. Boechler, G. Theocharis, and C. Daraio, "Bifurcation-based acoustic switching and rectification," Nat. Mater. **10**(9), 665–668 (2011).

86. A. Spadoni and C. Daraio, "Generation and control of sound bullets with a nonlinear acoustic lens.," Proc. Natl. Acad. Sci. U. S. A. **107**(16), 7230–4 (2010).

87. C. M. Donahue, P. W. J. Anzel, L. Bonanomi, T. A. Keller, and C. Daraio, "Experimental realization of a nonlinear acoustic lens with a tunable focus," Appl. Phys. Lett. **104**(1), 014103 (2014).

88. M. A. Porter, P. G. Kevrekidis, and C. Daraio, "Granular crystals: Nonlinear dynamics

meets materials engineering," Phys. Today **68**(11), 44–50 (2015).

89. W.-H. Lin, "Dynamic Characterization of Micro-Particle Systems," California Institute of Technology (2016).

90. N. V. Dziomkina and G. J. Vancso, "Colloidal crystal assembly on topologically patterned templates," Soft Matter **1**(4), 265 (2005).

91. L. Braginsky and V. Shklover, "Light propagation in an imperfect photonic crystal," Phys. Rev. B **73**(8), 085107 (2006).

92. V. Mizeikis, S. Juodkazis, A. Marcinkevičius, S. Matsuo, and H. Misawa, "Tailoring and characterization of photonic crystals," J. Photochem. Photobiol. C Photochem. Rev. **2**(1), 35–69 (2001).

93. A. Khanolkar, S. Wallen, M. Abi Ghanem, J. Jenks, N. Vogel, and N. Boechler, "A self-assembled metamaterial for Lamb waves," Appl. Phys. Lett. **107**(7), 071903 (2015).

94. A. van Blaaderen and P. Wiltzius, "Growing large, well-oriented colloidal crystals," Adv. Mater. **9**(10), 833–835 (1997).

95. Y. Yin, Y. Lu, B. Gates, and Y. Xia, "Template-Assisted Self-Assembly: A Practical Route to Complex Aggregates of Monodispersed Colloids with Well-Defined Sizes, Shapes, and Structures," J. Am. Chem. Soc. **123**(36), 8718–8729 (2001).

96. Q. Chen, S. C. Bae, and S. Granick, "Directed self-assembly of a colloidal kagome lattice," Nature **469**(7330), 381–384 (2011).

97. M. Yoldi, W. González-ViñAs, M. C. Arcos, and R. Sirera, "Electrophoretic deposition of colloidal crystals assisted by hydrodynamic flows," J. Mater. Sci. **41**(10), 2965–2969 (2006).

98. A. Ashkin, "Acceleration and Trapping of Particles by Radiation Pressure," Phys. Rev. Lett. **24**(4), 156–159 (1970).

99. D. G. Grier and Y. Roichman, "Holographic optical trapping," Appl. Opt. **45**(5), 880 (2006).

100. K. Kyoko, I. Masato, M. Hajime, and N. Hayashi, "A Novel Water-Soluble Photoinitiator for the Acrylic Photopolymerization Type Resist System," Chem. Mater. **10**(11), 3429–3433 (1998).

101. S. Just and K. Pedersen, *Circular Hough Transform* (2007).

102. C. Hesseling, M. Woerdemann, A. Hermerschmidt, and C. Denz, "Controlling ghost traps in holographic optical tweezers," Opt. Lett. **36**(18), 3657 (2011).

103. R. W. Gerchberg and W. O. Saxton, "A practical algorithm for the determination of phase from image and diffraction plane pictures," Optik (Stuttg). **35**(2), 237–246 (1972).

104. P. S. Pundir, S. K. Porwal, and B. P. Singh, "A New Algorithm for Solving Linear Bottleneck Assignment Problem," J. Inst. Sci. Technol. **20**(2), 101–102 (2015).

105. H. W. Kuhn, "The Hungarian method for the assignment problem," in *Naval Research Logistics Quarterly* (1955), **2**(1–2), pp. 83–97.

106. L. A. Shaw, S. Chizari, and J. B. Hopkins, "Improving the throughput of automated holographic optical tweezers," Appl. Opt. **57**(22), 6396 (2018).

107. R. C. Ball and J. R. Melrose, "A simulation technique for many spheres in quasi-static motion under frame-invariant pair drag and Brownian forces," Phys. A Stat. Mech. its Appl. **247**(1–4), 444–472 (1997).

108. A. Kumar and J. J. L. Higdon, "Origins of the anomalous stress behavior in charged colloidal suspensions under shear," Phys. Rev. E - Stat. Nonlinear, Soft Matter Phys. **82**(5), 1–7 (2010).

109. B. Derjaguin and L. Landau, "Theory of the stability of strongly charged lyophobic sols and of the adhesion of strongly charged particles in solutions of electrolytes," Prog. Surf. Sci.

43(1–4), 30–59 (1993).

110. E. J. W. Verwey and J. T. G. Overbeek, "Theory of the Stability of Lyophobic Colloids," Nature **162**(4113), 315–316 (1948).

111. C. Gutsche, U. F. Keyser, K. Kegler, F. Kremer, and P. Linse, "Forces between single pairs of charged colloids in aqueous salt solutions," Phys. Rev. E - Stat. Nonlinear, Soft Matter Phys. **76**(3), 1–7 (2007).

112. J. Israelachvili, *Intermolecular and Surface Forces* (2011).

113. S. A. Safran and M. Schick, "*Statistical Thermodynamics of Surfaces, Interfaces, and Membranes*," Phys. Today **49**(5), 68–68 (1996).

114. J. C. Crocker and D. G. Grier, "Microscopic measurement of the pair interaction potential of charge-stabilized colloid," Phys. Rev. Lett. **73**(2), 352–355 (1994).

115. E. Allahyarov, E. Zaccarelli, Y. Levin, E. Trizac, and M. C. Barbosa, "Interaction between charged colloids in a low dielectric constant solvent Interaction between charged colloids in a low dielectric constant solvent," EPL **81**, 6–8 (2008).

116. G. Pesce, V. Lisbino, G. Rusciano, and A. Sasso, "Optical manipulation of charged microparticles in polar fluids," Electrophoresis **34**(22–23), 3141–3149 (2013).

117. B. Giera, L. A. Zepeda-Ruiz, A. J. Pascall, J. D. Kuntz, C. M. Spadaccini, and T. H. Weisgraber, "Mesoscale particle-based model of electrophoresis," J. Electrochem. Soc. **162**(11), D3030–D3035 (2015).

118. A. Ashkin, "Forces of a single-beam gradient laser trap on a dielectric sphere in the ray optics regime," Biophys. J. **61**(2), 569–582 (1992).

119. W. H. Wright, G. J. Sonek, and M. W. Berns, "Parametric study of the forces on microspheres held by optical tweezers," Appl. Opt. **33**(9), 1735 (1994).

120. A. A. Bui, A. B. Stilgoe, N. Khatibzadeh, T. A. Nieminen, M. W. Berns, and H. Rubinsztein-Dunlop, "Escape forces and trajectories in optical tweezers and their effect on calibration," Opt Express **23**(19), 24317–24330 (2015).

121. S. Grego, E. Arimondo, C. Frediani, D. Fisica, G. Nazionale, and S. Lorenzo, "Optical tweezers based on near infrared diode laser," J. Biomed. Opt. **2**(3), 332–339 (1997).

122. G. Thalhammer, L. Obmascher, and M. Ritsch-Marte, "Direct measurement of axial optical forces," Opt. Express **23**(5), 6112 (2015).

123. J. E. Melzer and E. McLeod, "Fundamental Limits of Optical Tweezer Nanoparticle Manipulation Speeds," ACS Nano **12**(3), 2440–2447 (2018).

124. S. Chizari, L. A. Shaw, and J. B. Hopkins, "Simultaneous printing and deformation of microsystems via two-photon lithography and holographic optical tweezers," Mater. Horizons **6**(2), 350–355 (2019).

125. M. D. Porter, B. Giera, R. M. Panas, L. A. Shaw, M. Shusteff, and J. B. Hopkins, "Experimental characterization and modeling of optical tweezer particle handling dynamics," Appl. Opt. **57**(22), 6565 (2018).

126. L. A. Shaw, S. Chizari, and J. B. Hopkins, "Improving the throughput of automated holographic optical tweezers," Appl. Opt. **57**(22), 6396 (2018).

127. T. A. Nieminen, N. du Preez-Wilkinson, A. B. Stilgoe, V. L. Y. Loke, A. A. M. Bui, and H. Rubinsztein-Dunlop, "Optical tweezers: Theory and modelling," J. Quant. Spectrosc. Radiat. Transf. **146**, 59–80 (2014).

128. M. Polin, K. Ladavac, S.-H. Lee, Y. Roichman, and D. G. Grier, "Optimized holographic optical traps," Opt. Express **13**(15), 5831 (2005).

129. Y. Song, R. M. Panas, and J. B. Hopkins, "A review of micromirror arrays," Precis. Eng.

51, 729–761 (2018).

130. J. B. Hopkins, R. M. Panas, Y. Song, and C. D. White, "A High-Speed Large-Range Tip-Tilt-Piston Micromirror Array," J. Microelectromechanical Syst. **26**(1), 196–205 (2017).